UNIVERSITY OF COPENHAGEN
FACULTY OF SCIENCE

MSc thesis report

The Solar Silicon Abundance

Niall Gray

Supervisors: Maria Bergemann, Troels Haugbølle, Åke Nordlund

Submitted: May 20, 2022

Abstract

The abundance of chemical elements in the Sun is a metric and a standard used in many aspects of astronomy, and as one of the most abundant metals, silicon is often used as an anchor point between the abundance scales corresponding to the solar photosphere and chondritic meteorites. Moreover, as one of the most important elements in solar evolution models, an accurate measurement of the silicon abundance is important in solving the *solar abundance problem*, a discrepancy between the canonical abundances and inferences from helioseimsology. A calculation of the photospheric solar silicon abundance using the MULTI3D radiative transfer code is thus presented, with description of the spectroscopic methods, 1D MARCS and 3D STAGGER model atmospheres and model atom data, and new observational data from Schäfer et al. (2020) employed. A comparison is made of the behaviour in spectral line production in 1D and 3D model atmospheres, and under local thermodynamic equilibrium (LTE) and non-local thermodynamic equilibrium (non-LTE) radiation transfer models terms of their equivalent widths, waveshifts, and asymmetry via bisectors. We present an original investigation of abundance calculations across the solar disk, in which we find challenges to the accuracy of simulations of the solar limb, and of the spatially resolved solar observations, nevertheless, we see remarkable consistency in line equivalent widths between 3D non-LTE modelling and observational data. Two sources of atomic transition probabilities are used to calculate the photospheric silicon abundance; values from the Kurucz database (Kurucz 2016) yield A(Si) = 7.61 dex, while new experimental values from Rhodin et al. (2018) produce A(Si) = 7.53 dex. It is shown that the calculated abundances are consistent across the solar disc. The compatibility of these results with recent studies is discussed, in the context of the impact of chemical abundances on astronomy and planetary science.

Contents

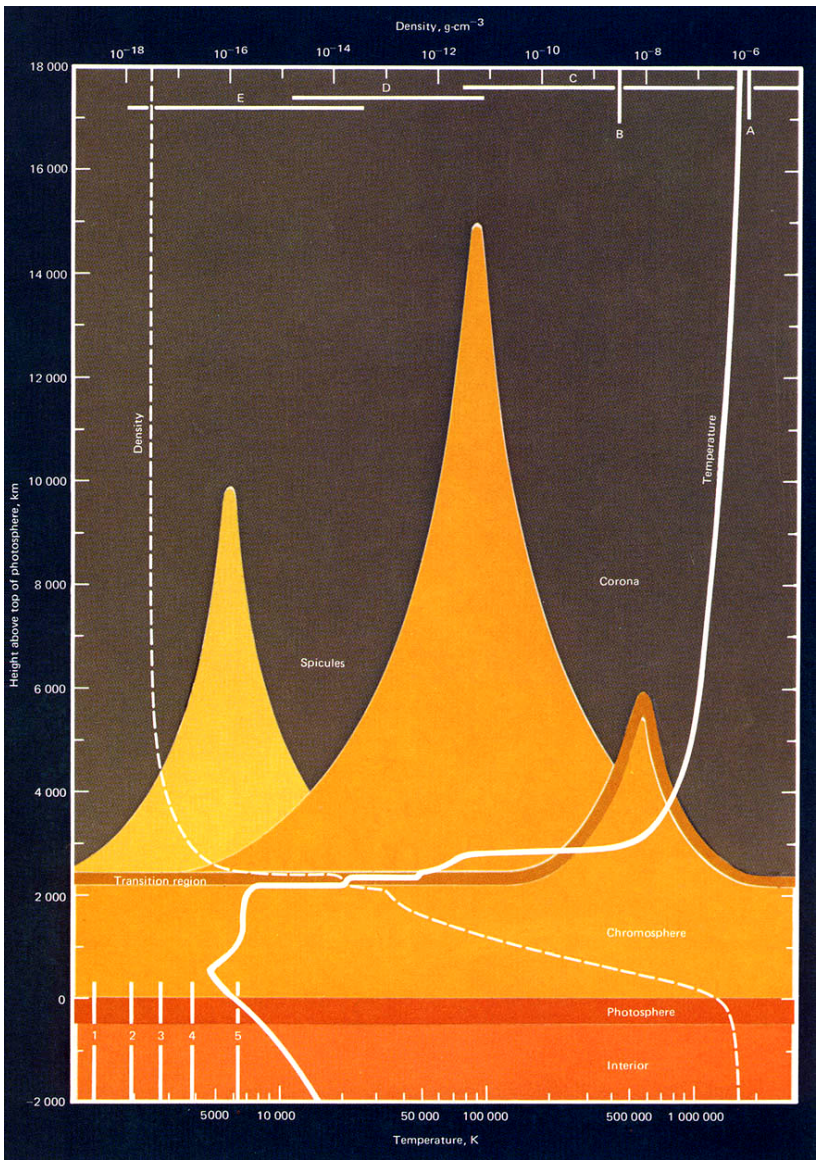

Figure 1: The solar atmosphere, from Eddy (1979).

1 Introduction

1.1 Motivation

Accurate measurement of solar abundances is a very important component in several astrophysical fields, as these abundances are a benchmark in the models which describe evolution and behaviour of planetary, stellar and galactic formation.

When we discuss the abundance of an element, it is common to use a logarithmic scale :

$$A(\mathrm{E}) = 12 + \log_{10}\frac{n(E)}{n(H)}$$

where E is the chemical element, and n(E) is the number of atoms of that element. The scale is relative to $n(\mathrm{H}) = 10^{12}$ atoms of hydrogen, the predominant element in the Sun (and the universe). In this work we often refer to the abundance in terms of 'dex', which are decadic logarithmic units, i.e., a factor of 2 dex is equal to a factor of 10^2 (Lodders 2019). There are a number of sources from which to estimate the relative abundance of elements, but there are few which have a representative mixture of the Sun. Here, we talk about 'CI chondritic meteorites', which are a variety of meteorite which have not 'differentiated', i.e., melted and separated into silicate and metal parts. These meteorites are dated to the early Solar System, and their chemical integrity means that the relative proportion of their metals is preserved, and assumed to match that of the outer layers of the present day Sun. It is from these outer layers that the evidence of solar abundances used in this study emanate, in the form of spectral radiation. The Sun's photosphere, which is the upper layer of the Sun's convective envelope, contains the 'surface' of the star, and it is from here that most of the light that leaves the Sun, escapes. This light is affected by the composition of the material through which it travels, and from which it is emitted, meaning that we may infer the proportion of chemicals present in the material by way of examining the emitted radiative spectrum. Abundances inferred from these spectroscopic methods are known as photospheric, or solar abundances.

Silicon is often used as a reference point to connect the chemical abundances of chondritic meteorites with the relative abundances associated with the solar photosphere (eg. Asplund et al. (2009)); these proportions are referred to as element/Si ratios (Lodders et al. (2009)), or the cosmochemical abundance scale, where atomic abundances are normalised to the number of silicon atoms, N(Si) = 10^6 (Lodders (2019)). A more practical reference element than more abundant but volatile elements such as hydrogen and oxygen, the condensation behaviour of silicon means that it is often present in meteorites and interstellar dust grains and as such, normalisation with Si was introduced by Goldschmidt (1937). The chemical abundances in CI chondrites have been considered to be largely consistent with that of the solar photosphere (Palme et al. (2014) report better than ±10% agreement for the majority of elements), which suggests that these two environments have preserved the 'primitive' composition of the early Solar System. This is in contrast to the chemical abundances in the Earth's crust, where melting of the mantle has separated its composite chemicals into local distributions unrepresentative of the early solar system. The use of mass spectrometry has allowed for the highly precise direct measurement of solar abundances, meaning that uncertainties in abundances stem primarily from photospheric calculations. For silicon, (Lodders et al. (2009)) quote 0.06 dex and 0.01 dex uncertainties for solar photospheric and CI chondrite abundances respectively. The use of both methods is necessary, partly due to the deficit of volatile elements in meteorites, and the depletion of lithium in the solar photosphere due to burning in the stellar interior, an abundance difference of a factor of 150 to that of meteorites Lodders et al. (2009), Asplund et al. (2009). Indeed, Asplund et al. (2021) lately report a correlation between the photospheric-chondritic abundance difference and condensation temperature, meaning that CI chondrites do not perfectly match with the composition of the Sun, and hence suggest that it is unwise to rely on the long-standing assumption that the abundances of CI chondrites are consistent with the photospheric abundance.

In the core accretion theory of planet formation, silicate grains with icy mantles form much of the solid material in the core of giant planets (Robinson et al. 2006). In a study on the relationship between Si abundance in stars and their likelihood to be giant planet hosts, Brugamyer et al. (2010) conclude that silicon (over oxygen) is the limiting reagent for grain nucleation, meaning that accurate knowledge of silicon abundance in stars is highly important to understanding the structure of their planetary systems. Brugamyer et al. (2010) calculate a relative, differential Si abundance between their sample stars, which are independent of exact solar silicon abundance calculations. However their abundance analysis follow solar studies such as Shi et al. (2008), which suggest that non-local thermodynamic equilibrium (non-LTE) effects in the stars are negligible for Si I abundance. It is important to follow up on these assumptions with more accurate atomic and 3D atmospheric models; if recent work shows that these non-LTE effects are in fact significant, then there is a knock-on effect to planetary research.

The findings of Brugamyer et al. (2010) concerning giant planets are corroborated by Adibekyan et al. (2012) via calculation of abundances of a number of elements including Si in a survey of 1111 FGK dwarf stars; they also find an enhancement in the [Si/Fe] ratio in host stars in the low-iron regime. A subset of this same sample was then used by Adibekyan et al. (2015) in a study focussed on the [Mg/Si] ratio, including only the dwarf stars with both effective temperature within 500K of the Sun, and estimated abundance uncertainty for Si, Mg and Fe less than 0.2 dex. They not only conclude that low-mass planets are more common around stars with a high [Mg/Si], but also that the relationship between the [Mg/Si] ratio and the metallicity of the star has an influence on the internal structure of terrestrial planets. The location and era of the formation of these stars is hence connected to the the composition of the their corresponding planets via the [Mg/Si] ratio, due to the placement of sites of Si production mechanisms in the galaxy. In particular, Adibekyan et al. (2015) and Haywood (2008) find that terrestrial planet-host stars are more common in the galactic thick disc than the thin disc, where the thick disc

contains stars with higher [Mg/Si] ratio. This ratio controls the distribution of silicates in rocky planets, influencing the characteristics of a large proportion of the mantle and crust of planets such as Earth, Venus and Mars, as detailed by Thiabaud et al. (2014). The consequences of inclusion of non-LTE effects in the calculation of [Mg/Si] may be of particular importance due to the difference in behaviour of the synthesised spectral lines from such studies. In an investigation into the Mg abundances in six Gaia stars via LTE and non-LTE model atmospheres, Bergemann et al. (2017) show that the stronger lines are brighter in LTE than non-LTE, in spatially averaged 3D ($\langle$3D$\rangle$) model atmospheres. This contrasts with the findings of Amarsi & Asplund (2017), where there is strengthening of spectral lines under non-LTE. Hence, development of 3D non-LTE model atmospheres may have a pronounced effect on studies which use [Mg/Si] as a diagnostic, such as those mentioned above.

Silicon is produced primarily through hydrostatic oxygen burning in massive stars and is then ejected in core-collapse supernovae. (Woosley (1995)). At the end of the carbon and oxygen burning phases, ^{28}Si is one of the dominant nuclei in the massive star, along with ^{32}S (Clayton (1983)). In the explosive stages of core-collapse, the so-called α-elements (O, Mg, Si, S, Ca) accept α particles, permitting the formation of a ladder of heavier elements up to the iron group. ^{28}Si nuclei are tightly bound, and their slow rate of photodisintegration and the abundance of ^{28}Si control the rate of the production of the iron group; this rate is also highly temperature dependent (Clayton (1983)). The different but interdependent production mechanisms of Si and Fe lead us to use the ratio of Si to Fe abundance to infer constraints on the physical structure of exploding massive stars. The ratio of α-elements to Fe also is indicative of the process of stellar evolution, i.e. the type of, and how many supernovae lead to the formation of present day stars in the Milky Way and other galaxies (Kobayashi (2016)). For example, Kobayashi et al. (2020) show through observations that the [Si/Fe] ratio is almost constant across stars of different ages and metallicities in the Milky Way.

Stars of different metallicities are expected to be distributed non-uniformly in the galaxy; old, metal-poor stars have a higher probability of being found in the inner galactic bulge, the oldest part of the galaxy. Studies into the chemical abundances of silicon and the other α-elements in these stars such as Howes et al. (2016), have helped confirm their metal-poor status, and investigate the chemical differences between similar stars in the galactic halo. Incorporating stars in surviving dwarf galaxies into the comparison between inner bulge and halo metal-poor stars, Reggiani et al. (2020) carry out a comparable study, relating abundances to differences in chemical evolution. They suggest that this may provide clues to answer some questions in galactic archaeology; the presence of metal-poor stars in regions of the galaxy where there is thought to have been rapid star formation in the formation of the bulge itself, and the presence of relatively rare types of supernovae enabled by this same process are linked by factors which should be deductible via abundance comparison studies. For example, they suggest that the relatively high [Si/Fe] $\sim$ +0.7 dex for their most metal-poor giant star is indicative of an oxygen-rich environment during nucleosynthesis. The authors also compare their calculated Si abundances between the halo dwarfs and giant stars in terms of the necessity of non-LTE abundance corrections; as the stellar parameters dictate the importance of these corrections in either case, their accurate calculation is key to proper comparisons between star classes in such cases.

Considering metal-poor stars which do happen to be found in the galactic halo, abundance analysis such as that by Yong et al. (2012) look at the relationships: [X/Fe] versus [Fe/H], mean abundance for relative elements, and [X/Fe] versus effective temperature, for relevant elements X (including Si). They compare these relations for dwarf and giant metal-poor stars, identifying some 'abundance peculiarities' (such as a star with an unusually high [Si/Fe] ratio) and, again, adding insight to the nature of the star's formation and progenitors.

With the physical parameters of the Sun, one can form standard solar models (SSMs), which are used to predict and describe various aspects

of the Sun's behaviour, properties and evolution. One example of this is the solar neutrino flux. In the Sun and other stars, silicon plays an important role in governing the radiative opacity in the stellar interior which in turn directly influences the local temperature. This temperature is a component in the rates of pp-chain and CNO-cycle fusion, mechanisms which are some of the sources of neutrino flux observed on Earth (in experiments such as Hosaka et al. (2006)). Publications of solar abundances through photospheric and meteoric analyses (such as Asplund et al. (2009), Caffau et al. (2010) and Scott et al. (2014)) have direct influence on the solar models with which the solar neutrino flux is compared. In Serenelli (2016) the author compares the stellar temperatures consistent with SSMs which correspond to these three solar abundance studies. Stellar temperature dictates which of the pp-chain branches, describing different fusion reactions with associated cross-sections, is dominant in the star (Adelberger et al. (2011)). The changes in the estimates of the abundance of the refractory elements and hence the metallicity of the Sun affect the agreement between helioseismology data and the solar models which depend partly on the photospheric and meteoric abundances. This issue has been dubbed *the solar abundance problem* (Serenelli (2016)) or *the solar modelling problem*, and is discussed in detail by Asplund et al. (2021).

For silicon in particular, the solar abundance has changed with the emergence of new data and methods of analysis. Grevesse & Sauval (1998) reported the value of A(Si) = 7.55 dex based on their methods with 1D LTE, but the canonical value was revised downwards to A(Si) = 7.51 dex with the introduction of 3D models (Asplund 2000). This value survives through to Amarsi & Asplund (2017), who use a full 3D hydrodynamic model atmosphere and updated atomic data. More recently however, new atomic and observational data have prompted a trend of slight increases in relative abundance of multiple elements, such as in oxygen (Bergemann et al. 2021); the latest photospheric silicon abundance is A(Si) = 7.59 dex from Magg et al. (2022).

When observing the Sun, it is possible to record spectra emitted from

certain parts of the solar surface. The spectral lines from these spatially resolved intensities vary as one looks across the solar disc, behaviour we would wish to replicate accurately in synthesised spectra. We have seen centre-to-limb solar abundance studies of some chemicals, such as iron Lind et al. (2017) and oxygen Bergemann et al. (2021), but none, as yet, for silicon with full 3D non-LTE modelling.

1.2 Aims of this work

Following recent developments, we wish to investigate the photospheric silicon abundance with the latest atomic and observational data and with a modern 3D hydrodynamic model atmosphere. We will use MULTI3D Leenaarts & Carlsson (2009) to solve the radiative transfer and statistical equilibrium equations in LTE and non-LTE, and to synthesis spectra with the calculated level populations. The spectra produced in a 1D model atmosphere (Gustafsson et al. 2008) will be compared to modelling in full 3D (Magic et al. 2013). With the availability of spatially resolved solar data from Schäfer et al. (2020), we will for the first time investigate the distribution of calculated Si abundances across the solar disc, and with this assess the performance of the spectral synthesis methods at the solar limb. At the conclusion of this work, we will address the findings of the study in terms of the solar abundance problem, and in the context of similar studies.

2 LTE and Non-LTE radiative transfer

In order to perform abundance analysis, one requires synthesised radiation spectra with which to compare the observed data. An element of this synthesis is based on the assumption known as local thermodynamic equilibrium, a theory to simplify complex radiative transfer to a more computationally tractable problem. This is a simplification it was necessary to take for many years, before advances in computation made it possible to model radiation transfer in more accurate detail, so called non-LTE. There are still some situations in which LTE is a reasonable assumption, and due to its modest computational economy we perform our analysis in both regimes. Here we present some of the theory underpinning the simulations of radiative transfer and then LTE and non-LTE in particular.

2.1 Radiative transfer and line formation

Understanding of the physical processes through which electromagnetic radiation travels through the upper regions of a star is required not only to be able to model the processes computationally, but also to be able to understand the radiation which we observe from the ground, or via satellite telescopes. These processes are described by the theory of radiative transfer; the formalism here follows that of Mihalas (1978) and Rutten et al. (1995).

The first quantity to define is the specific intensity, I_ν, which is the amount of energy at frequency ν which passes through an area perpendicular to the direction of travel of the beam, per unit time per solid angle. As wish to understand the passage of light through the atmosphere, we are interested in the equation of radiative transfer, which describes the evolution of the radiation field I_ν along its path through the medium. The time-dependent radiative transfer equation is:

$$\frac{1}{c}\frac{dI_\nu}{dt} + \frac{dI_\nu}{ds} = j_\nu \rho - \kappa_\nu \rho I_\nu \tag{1}$$

where κ_ν and j_ν are the absorption coefficient and emission coefficient of

the propagation medium, both per unit mass, and ρ is the mass density of the medium. ds is the geometric path length in the same direction as the beam, t is time, and c is the speed of light. At the time scales of the processes here, the photon interactions and that of the movement of the medium, are far removed, meaning that we do not expect the radiation field to vary over time, so we may assume that the dynamics is *quasi-static* and ignore the time dependent term.

If we approximate a plane-parallel atmosphere, the atmosphere is considered to be a set of parallel layers, wherein the conditions in each individual layer are constant, so that the physical properties only vary in the vertical direction. As this ignores the curvature of the body, the plane-parallel approximation requires that the atmosphere is a relatively thin layer around the body. For the solar photosphere this is not too far a stretch, as it makes up just 0.014% the radius of the Sun. A consequence of this is that the path length of the beam can be written as

$$ds = -\frac{dz}{\mu} = -\frac{d\tau}{\mu\kappa\rho} \tag{2}$$

where z defines the vertical depth perpendicular to the plane, μ the cosine of the angle between z and s, κ the opacity, ρ the matter density and τ is a quantity called the optical depth. The negative sign in Eqn. 2 defines the optical depth as increasing towards the centre of the star, such that $\tau_\nu \sim 1$ corresponds to the 'surface', the point at which the matter becomes opaque to radiation of frequency ν. This point varies significantly with frequency, meaning that the place of origin in the star of a spectral line varies from line to line, and even within the elements of a single line.

A form of the radiative transfer equation with this angular dependence is:

$$\mu\frac{dI_\nu}{d\tau} = I_\nu - S_\nu \tag{3}$$

S_ν is the source function, which is characteristic of the stellar atmosphere. In the simple LTE case it can be considered equal to the Planck function $B_\nu(T)$ (Equation 10), and if scattering is not considered it is the

ratio of the emissivity and absorption coefficients. Following Kirchoff's law of thermal emission we have:

$$S_\nu = B_\nu(T) = \frac{j_\nu}{\kappa_\nu} \tag{4}$$

If instead we do include the extinction due to scattering rate κ_s, then the source function is

$$S_\nu = \frac{\kappa_\nu B_\nu(T) + \kappa_\nu J_\nu}{\kappa_\nu + \kappa_s} \tag{5}$$

where J_ν is the mean intensity averaged over all solid angles:

$$J_\nu = \frac{1}{4\pi} \int_\Omega I_\nu \, d\Omega. \tag{6}$$

The radiative transfer equation can also be written for the specific intensity, by integrating over the optical depth (Bergemann & Nordlander 2014) as:

$$I_\nu(\tau_\nu = 0) = \int_0^\infty S_\nu(\tau_\nu) \, e^{-\tau_\nu} d\tau_\nu \tag{7}$$

If one again assumes a plain parallel atmosphere, then the angle specific intensity is:

$$I_\nu(\tau_\nu = 0, \mu) = \int_0^\infty S_\nu(\tau_\nu) \, e^{-\tau_\nu/\mu} \frac{d\tau_\nu}{\mu} \tag{8}$$

In many studies, particularly in those concerning unresolvable non-Sun stars, the next step is to integrate over μ to generate the apparent flux of the star. Instead, due to the proximity of the Sun, we are in a position to calculate the intensities specific to arbitrary angles on the Sun, and compare these with the corresponding measurements of the observed spectra.

There are four main sources of opacity in stellar atmospheres, which are:

Bound-bound transitions are transitions between the energy levels of an atom which correspond to discrete absorption or emission of radiation.

Bound-free absorption, or *photoionisation*, involves the absorption of a photon by an atom in a bound state, causing the emission of an electron into the continuum. The emitted electron has energy equal to the difference between its ionisation potential and the incident photon.

Free-free absorption is the process in which a photon is absorbed by a free electron and a free ion, which subsequently radiate.

The latter two of these processes are continuous, as they contribute opacity over large frequency ranges, relative to the absorption lines, and thus form a continuum intensity. The opacity contributed by each atom species through the continuum processes is weighted by the abundance of the atoms in the atmosphere, giving a frequency dependent continuum absorption coefficient $\kappa_{C\nu}$.

One can form the synthesised spectra with the source functions, and the opacities, or absorption coefficients, κ_ν. This frequency specific absorption coefficient is a combination of the all contributions of absorption coefficients corresponding to spectra lines which have significant intensity at the observed frequency, κ_L, and the absorption coefficient of the continuous processes, κ_C. If each line corresponds to a transition between lower level i and upper level j, then the total opacity is given by:

$$\kappa_\nu = \sum_{ij} \kappa_{L\nu}(ij) + \kappa_C \tag{9}$$

2.2 LTE

In LTE, the state of the matter in the gas is dependent wholly on the local temperature and the total particle density. The particles exist in thermal equilibrium in their own local region, and the local temperature, T, is general in that it applies in the calculation spectral radiance, particle velocity distribution and atomic excitation and ionisation levels.

In LTE, the source function S_ν is given by the black-body Planck function B_ν, meaning that the inter-particle interactions are not coupled with the intensity field, thus the spectral radiance is determined only by the temperature, T:

$$B_\nu = \frac{2h\nu^3}{c^2}\frac{1}{e^{h\nu/kT} - 1} \tag{10}$$

where k is Boltzmann's constant and h is Planck's constant.

In order to compute the collisonal rates, one must first learn the velocities of the colliding particles in the material. In equilibrium, the velocities of the matter particles in the gas relax to a predictable distribution, with disregard of course to non-elastic collisons, van der Waals interactions, and other effects. This is described by the Maxwell-Boltzmann distribution:

$$N(V)dV = \left(\frac{M}{2\pi kT}\right)^{3/2} e^{-\frac{MV^2}{2kT}} dV \tag{11}$$

for N, the number of particles of mass M moving between speeds of V and dV. The Boltzmann equation describes the distribution of species of atoms in different ionisation stages relative to their ground state. This fraction is:

$$\frac{N_n}{N} = \frac{g_n}{Z} e^{-E_n/kT} \tag{12}$$

where n denotes the excitation level with corresponding energy E_n given relative to the ground state energy and g_n is the statistical weight corresponding to this level. Z is the partition function, and acts as a normalisation factor:

$$Z = \sum_i g_i e^{-E_i/kT} \tag{13}$$

If instead we are interested in the fraction between the populations of two consecutive ionisation levels, we use Saha's equation:

$$\frac{N_{n+1}}{N_n} = \frac{1}{N_\mathrm{e}} \frac{2Z_{n+1}}{Z_n} \left(\frac{2\pi m_\mathrm{e} kT}{h^2} \right)^{3/2} \mathrm{e}^{-I/kT} \tag{14}$$

where N_e is the number density of electrons and m_e is the electron mass. I is the ionisation potential i.e., the energy needed to move from ionisation state n to state $n + 1$. Finally, the Boltzmann equation and the Saha equation can be combined into the Saha-Boltzmann distribution:

$$\frac{n_c}{n_i} = \frac{1}{N_\mathrm{e}} \frac{2g_c}{g_i} \left(\frac{2\pi m_\mathrm{e} kT}{h^2} \right)^{3/2} \mathrm{e}^{-E_{ci}/kT} \tag{15}$$

which gives the ratio of n_i, the number density of the population at level i, to n_c, the number of ions at ionisation state c. E_{ci} is the ionisation energy separating these two states.

2.3 Transitions and Non-LTE

We have considered the situation where LTE is a reasonable assumption; when the radiation field and the matter through which it passes are strongly thermally coupled, such as in the dense interior of a star. On the other hand, we may consider a location in which there is a much lower coupling; where the mean free path of a photon is sufficiently large, larger than the scale height of the material, such as at the stellar surface. One must consider non-LTE effects in order to realistically model radiative energy transfer in such situations, as in the solar photosphere.

If one reaches a situation where LTE can no longer be assumed, then the Planck function, Boltzmann equation, and Saha's equation can no longer be taken to accurately describe the radiation field, excitation distribution and ionisation state distribution. Instead, we use the Statistical Equilibrium (SE) equations, also known as rate or population equations,

which give a microscopic description of the interaction between the radiation field and the stellar gas. They imply that there is no change over time in these three distributions, and describe the rate at which, through some process, there is a transition from level i to level j per unit time.

In general, we have C_{ij} as the rate of transitions due to collisions and R_{ij} as the rate due to radiation. The total rate is then:

$$P_{ij} = C_{ij} + R_{ij} \tag{16}$$

and the number of transitions per unit volume is $n_i P_{ij}$, if n_i is again the level i particle number density. We can write the equilibrium equations as:

$$\frac{\mathrm{d}n_i}{\mathrm{d}t} = \sum_{j \neq i} n_j P_{ji} - n_i \sum_{j \neq i} P_{ij} = 0 \tag{17}$$

with which we also have particle conservation for n_t the total number of particles:

$$\sum_{j=1}^{n_l} n_j = n_t \tag{18}$$

Such an equilibrium equation exists for each level i for every ion in the atmosphere, and each is solved simultaneously in a radiative transfer code such as MULTI3D.

2.3.1 Radiative rates

The radiative rates are controlled by probabilities related to the processes which describe transition between states i and j. These three probabilities are the Einstein coefficients:

The Einstein coefficient for spontaneous emission A_{ji} is the probability per second of a spontaneous de-excitation of an atom from state $j \rightarrow i$ with the emission of a photon of energy $E_{ji} = h\nu_{ji}$. Then, the rate of

spontaneous decays per unit volume is $n_j A_{ji}$.

The Einstein coefficient for radiative absorption B_{ij} is the probability of atomic absorption of a photon corresponding to a transition of atomic states $i \rightarrow j$. The probability of radiative absorption for an atom in the radiation field I_ν is $B_{ij} I_\nu d\Omega$ for solid angle $d\Omega$.

The Einstein coefficient for stimulated emission B_{ji} is the probability of decay of an atom from state $j \rightarrow i$, stimulated by the presence of another photon, and the probability of stimulated emission in the field I_ν is similarly defined as $B_{ij} I_\nu d\Omega$. Again the emitted photon has the energy E_{ji}.

There exist quantum mechanical relationships between these coefficients, as:

$$A_{ji} = \frac{8\pi h\nu^3}{c^2} B_{ji} \tag{19}$$

$$B_{ij} = \frac{g_j}{g_i} B_{ji} \tag{20}$$

The general radiative rates can be given by the compact unified relations (Rutten et al. 1995) which account for the rates per particle of both the bound-bound (b-b) and bound-free (b-f) transitions.:

$$R_{ij} = \int_0^\infty \frac{4\pi}{h\nu} \sigma_{ij}(\nu) J_\nu d\nu \tag{21}$$

and

$$R_{ji} = \int_0^\infty \frac{4\pi}{h\nu} G_{ij} \sigma_{ij}(\nu) \left(\frac{2h\nu^3}{c^2} + J_\nu \right) d\nu \tag{22}$$

σ_{ij} and G_{ij} are defined for bound-bound and bound-free transitions as follows:

$$G_{ij} = \begin{cases} \left[\frac{n_i}{n_c}\right]_{LTE} \exp\left(-\frac{h\nu}{kT}\right) & \text{(b-f)} \\ g_i/g_j & \text{(b-b)} \end{cases} \tag{23}$$

and

$$\sigma_{ij} = \begin{cases} \sigma_{ic}(\nu) & \text{(b-f)} \\ \frac{h\nu_{ij}}{4\pi} B_{ij}\varphi_\nu & \text{(b-b)} \end{cases} \tag{24}$$

where $\sigma_{ic}(\nu)$ is the monochromatic bound-free extinction coefficient per particle and φ_ν is the normalised absorption profile at the frequency ν.

2.3.2 Collisional rates

The transition rates due to collisions depend on the local electron temperature and of the density of the particular species to be excited ($n_e(v)dv$). Therefore, we have the excitation rate:

$$C_{ij} = \int_{v_0}^{\infty} n_c \sigma_{ij}(v) v f(v) dv \tag{25}$$

and de-excitation rate:

$$C_{ij} = n_e \int_{0}^{\infty} n_c \sigma_{ji}(v) v f(v) dv \tag{26}$$

where $f(v)$ is the Maxwellian velocity distribution, σ is the collisional cross-section and v_0 is the the threshold velocity given by

$$1/2 m v_0^2 = h\nu$$

with m the reduced mass of the colliding particle.

2.3.3 Line formation

In the cases where non-LTE is important and must be included in the radiation transfer models to accurately describe the stellar atmosphere, it is common that a small number of processes dominate the effects. We may focus on these channels to access the contribution of non-LTE effects. This is done quantitatively using level departure coefficients, b_i, which are simply ratios of the level populations in LTE and non-LTE in terms of their number densities (Bergemann et al. 2017):

$$b_i = n_i^{(non-LTE)}/n_i^{(LTE)} \tag{27}$$

We may use this ratio to define some terms for the particular levels in LTE and non-LTE conditions ie. $b_i = 1$ in LTE, and we may say that the level i is *thermalised*, and obeys the Saha-Boltzmann statistics. In non-LTE, one can say that the level i is *overpopulated* when $b_i > 1$ and is *underpopulated* when $b_i < 1$.

We may now examine the major channels through which we may obtain values for the departure coefficients (Bergemann 2014):

Over-recombination: In the case that the mean intensity is smaller than the Planck function, $J_\nu < B_\nu$, the upper levels experience a over-recombination due to the lack of ionisation.

Photoionisation and photon pumping: In the case that the mean intensity is larger than the Planck function, $J_\nu > B_\nu$, then we see over-ionisation and over-excitation, which is also known as photon pumping.

Photon loss: In the parts of the atmospheric layers where the optical depth is below unity, there is escape of photons beyond the boundary of the stellar atmosphere, causing a deficit in the levels of radiative excitation (in terms of the statistical equilibrium equations). This leads to over-population of the lower energy levels, also because of spontaneous de-excitations from the upper levels.

Photon suction: In layers where the optical depth is below unity, photon suction describes a succession of de-excitations via spontaneous transitions due to photon loss in near-infrared lines (Rutten et al. 1995). The succession of transitions in this process connect the upper and lower energy levels of the atom.

In nature these processes are not usually easy to parse, but we can further reduce our view on the dominant channels by dividing atoms into either photoionisation dominated atoms or collision-dominated ions (Bergemann (2014), Gehren et al. (2001)). Si I belongs to the former group, meaning that the leading cause of non-LTE is over-ionisation, the resulting underpopulated levels lead one to expect departure coefficients $b_i < 1$.

In non-LTE the atomic level and ionisation stage populations in the medium influence and are influenced by the non local radiative field, meaning that the radiative transfer equations and statistical equilibrium equations must be solved simultaneously. The emission coefficient is defined with the Einstein coefficients as:

$$j_\nu^l = \frac{h\nu}{4\pi} n_j A_{ji} \varphi_\nu \tag{28}$$

The extinction coefficient of a given spectral line depends on the populations and statistical weights corresponding to the transition with frequency ν:

$$\kappa_\nu^l \rho = n_i \left(1 - \frac{n_j g_i}{n_i g_j}\right) h\nu \tag{29}$$

Due to historical reasons, in astronomical spectroscopy the Einstein coefficients are often replaced by a parameter known as *f-value*, or oscillator strength. This is related to the Einstein absorption coefficient as:

$$n_i B_{ij} = n_i \frac{1}{h\nu} \frac{\pi e^2}{4\pi\epsilon_0 m_e c} f = \int \kappa_\nu^l \rho \, \mathrm{d}\nu \varphi_\nu \tag{30}$$

with the electron mass m_e and vacuum permittivity ϵ_0.

To calculate the intensity at each frequency with Eqn. 8, the line source function in non-LTE can now be used, which reduces to the Planck function when $b_i = 1$. We can use the the level populations to calculate S_ν^l with the equation:

$$S_\nu^l = \frac{\kappa_\nu^l}{j_\nu^l} = \frac{2h\nu^3}{c^2} \frac{1}{\frac{n_i g_j}{n_j g_i} - 1}. \tag{31}$$

Due to its discrete nature, one may expect the spectral line corresponding to an atomic transition to be a δ-function. However, there are a series of phenomena which *broaden* the lines, forming the line profiles we observe. The first of these is Doppler broadening, which is caused by the relative velocity of a radiating particle in the line of sight, due to thermal motion, or small scale motion due oscillations and streaming motions (Emerson 1998), known as microturbulence. The Gaussian distribution of Doppler shifted frequencies around the central transition frequency ν_0, is:

$$\varphi(\nu) = \frac{1}{\sqrt{\pi}\Delta\nu_D} e^{-(\Delta\nu/\Delta\nu_D)^2} \tag{32}$$

where $\Delta\nu_D$ is the Doppler width, defined as:

$$\Delta\nu_D = \frac{\nu_0}{c} \sqrt{\frac{2kT}{m} + \xi_t^2}. \tag{33}$$

The parameter ξ_t is non-zero when microturbulence is specified. There exists an intrinsic width in a spectral line, which is called natural line broadening. This is due to the spread in the energy of an exited atomic state following Heisenberg's uncertainty principle, $\Delta E \Delta t \sim h/(2\pi)$, where t is the lifetime of the state. A further source of line broadening is due to collisions of the radiating particle with other particles, such as electrons. The distribution of frequencies due to these effects is a Lorentzian profile:

$$\varphi(\nu) = \frac{\Gamma}{4\pi^2} \frac{1}{(\Delta\nu)^2 + (\Gamma/4\pi)^2} \tag{34}$$

where Γ is the sum of the natural and collisional line widths. Combining the sources of line broadening involves convolving the corresponding Gaussian and Lorentzian profiles. The result is known as a Voigt profile.

3 Model atmospheres

In order to simulate the radiative transfer behaviour in the atmosphere in the Sun, we require a model describing the physical nature of the matter through which the radiation travels. This is in general a picture of the stellar structure; a map of the relevant physical parameters in a representative space corresponding to our choice of geometry. For reasons leaning on computational demands explained later, it is necessary for us to obtain a model of the stellar atmosphere in both a one-dimensional format, as well as the more complex and physically accurate 'full' 3D picture.

3.1 1D Models

In the case of the 1D atmosphere, we selected an iteration of the MARCS grid of stellar models (Gustafsson et al. (2008), Henyey et al. (1965)). In MARCS atmospheres, LTE, hydrostatic equilibrium and flux constancy are assumed to hold. Further, they incorporate the Mixing-Length Theory (MLT), wherein turbulent convection is involved in energy transfer in the solar convective zone via a parameter ℓ, the mixing length (Nordlund et al. (2009)). This describes the characteristic distance which a 'parcel' of fluid moves in an up- or down-flow, before its characteristics match those of its surroundings. The convective flux is given by the ratio of the mixing-length parameter α_{MLT} to the pressure scale height H_p: $F_{con} \sim \frac{\alpha_{MLT}}{H_p}$. The total stellar energy flux is this convective flux added to the radiative flux :

$$F = F_{\text{con}} + F_{\text{rad}} = \frac{L}{4\pi r^2} \tag{35}$$

which influences our synthetic spectra through the luminosity L, which controls the star's effective temperature. However, MLT is no longer accepted as an accurate model, and in the description of 3D atmospheres we will see how this approach to energy transfer is replaced.

There are a number of key equations relating to hydrostatic equilibrium radiation transfer which must are solved when computing MARCS

solar atmosphere models, a selection of which are discussed in the following section; we follow some of the formalism from Bergemann (2014), Rutten et al. (1995), Emerson (1998) and Gustafsson et al. (2008).
The equation of hydrostatic equilibrium is given by:

$$\nabla P_{\text{tot}} = -\rho \frac{GM_r}{r^2} \tag{36}$$

where G is the Newtonian constant of gravitation, M_r is the mass contained within the radius r and P_{tot} is the total pressure. This is made up of:

$$\nabla P_{\text{tot}} = \nabla P_{\text{rad}} + \nabla P_{\text{gas}} + \nabla P_{\text{turb}} \tag{37}$$

where ∇P_{rad} is the force exerted on the stellar material by the radiation field and can be written as:

$$\nabla P_{\text{rad}} = -\frac{1}{c} \int_0^\infty (\kappa_\nu + \sigma_\nu) F_\nu d\nu \tag{38}$$

with κ_ν and σ_ν the absorption and scattering coefficients, and F_ν the monochromatic flux. ∇P_{rad} and the ∇P_{gas} balance the force due to the star's self-gravitation, while the turbulent pressure is due to the turbulent or convective movements of the gas. It may be modelled as $\nabla P_{\text{turb}} = \beta \rho v^2$, where β is a parameter of the order unity, and v is a characteristic velocity. This velocity is difficult to ascertain, and in MARCS, various approximations are used to arrive at a method which mirrors the effects of the turbulent and radiative pressures by adapting the local surface gravity, $g(r)$, where $g(r) = \frac{GM_r}{r^2}$ (Gustafsson et al. 2008).

MARCS uses the LTE equations described earlier to calculate the populations of atomic levels and excitation states in the atmosphere. Deep in the atmosphere much of the energy transfer is due to convective flux, but often $F_{conv} = 0$ in upper layers of the model (Gustafsson et al. 2008). When under the assumption that radiation is the only mechanism for energy transport in the atmosphere, it is necessary to describe the equilibrium between the 'sinks' and 'sources' of radiation in our system. These are namely the mean intensity and source functions as just described, as shown in the radiative equilibrium equation:

$$\int_0^\infty \kappa_\nu J_\nu(\tau) d\nu = \int_0^\infty \kappa_\nu S_\nu(\tau) d\nu. \tag{39}$$

In the description of MLT we saw that the total stellar flux is a combination of the radiative and convective fluxes. We also know that the emergent flux obeys the Stefan-Boltzmann law, which is linked to the flux in the equation for flux constancy:

$$F = \frac{L}{4\pi R^2} = \sigma T_{\rm eff}^4 \tag{40}$$

where $T_{\rm eff}$ is the effective temperature and σ is the Stefan-Boltzmann constant. In this approach the Sun is approximated to radiate like a black body.

With the physics discussed above, Gustafsson et al. (2008) produced a grid of 1D stellar atmosphere models covering an array of parameter ranges. We select such a 'snapshot' with those parameters which match the Sun, and reuse this as input for all the 1D spectrum synthesis, without needing to simulate the atmosphere as a step in our analysis, which would be extremely computationally expensive. The MARCS snapshot consists of a list describing a 1D column which is vertical in the atmosphere, and denotes the temperature, pressure and optical depth. In order to work with inclined viewing angles through the atmosphere, it is necessary to extend this model a plane-parallel structure with homogeneous 'slabs'.

The MARCS atmosphere used in this study is the same as used in Bergemann et al. (2019) and Bergemann et al. (2021), with microturbulence parameter $\xi_t = 1 \text{km s}^{-1}$ and $\alpha_{MLT} = 0.5$.

3.2 3D Models

Due to progression in numerical modelling, it is relatively recently that stellar modelling in 3D and radiative hydrodynamics (RHD) has been

deemed feasible for this variety of analysis. This family of models largely moves away from some of the simplifications discussed in the previous section, such as MLT and hydrostaticity. Instead, these models incorporate complex convective and turbulent behaviour in the stellar interior, phenomena which are not introduced manually to the model but arise naturally from the time-dependent hydrodynamic equations (Magic et al. 2013).

The second model atmosphere we use is one in the STAGGER-grid, built with the STAGGER-code, a 3D radiation magneto-hydrodynamics FORTRAN code which includes convective motions and turbulent flows (Nordlund et al. 2009). It aims to achieve a more realistic approximation of radiative transfer (Magic et al. 2013) than the corresponding 1D models, in cool late-type stars. The STAGGER-code was written to be highly parallelisable, allowing for use on modern high performance compute clusters. The grid covers a wide range of stellar parameters including effective temperature, metallicity, and surface gravity. We use the same snapshot as Bergemann et al. (2021), which covers 8×8 Mm in the horizontal, and runs from ~ 3 Mm below the optical surface to 9 Mm above. The snapshot has a resolution of $240 \times 240 \times 230$, which was reduced in the horizontal axes to $30 \times 30 \times 230$, following tests by Bergemann et al. (2021) that show the effect of this down-scaling is negligible. For illustration, we show part of our snapshot represented for parameters gas temperature (Fig. 2) and vertical velocity (Fig. 3). In some studies a so-called $\langle 3D \rangle$ model atmosphere is used, which is a temporally and spatially averaged 3D model and decreases the radiation transfer computational time, but is a less realistic picture, and was not used in this study; instead we use a snapshot in 'full 3D'.

The code solves numerically the radiative-hydrodynamic (RHD) equations, that is, the time evolution of the hydrodynamical macroscopic properties of fluids, and additionally their extension to include the optical properties of the plasma, and incorporates modelling of subsurface convection. These are the equations for the mass conservation (continuity

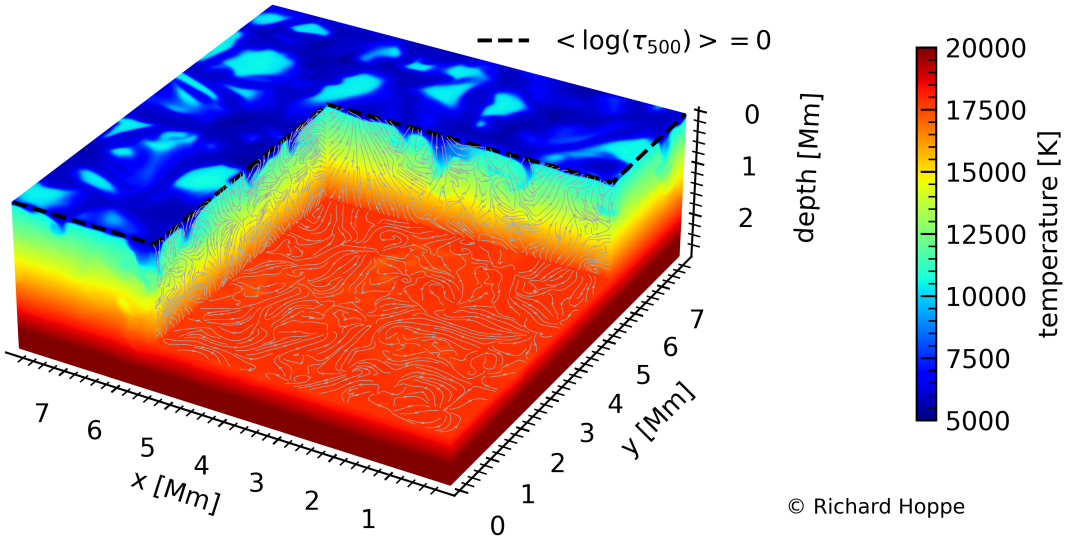

Figure 2: Snapshot of STAGGER model atmosphere showing the distribution of temperature. The upper bound is the optical depth where $\log\tau_{500} \approx 0$. Reproduced with permission from Bergemann et al. (2021).

equation), momentum conservation and energy conservation.

$$\frac{\partial \rho}{\partial t} + \nabla \cdot (\rho \boldsymbol{v}) = 0 \tag{41}$$

$$\frac{\partial \rho \boldsymbol{v}}{\partial t} + \nabla \cdot (\rho \boldsymbol{v}\boldsymbol{v} + \tau_{\text{visc}}) + \nabla P - \rho \boldsymbol{g} = 0 \tag{42}$$

$$\frac{\partial \epsilon}{\partial t} + \nabla \cdot (\epsilon \boldsymbol{v}) + P(\nabla \cdot \boldsymbol{v}) - Q_{\text{rad}} - Q_{\text{visc}} \tag{43}$$

where Q_{rad} is the heating or cooling per unit volume, solved from the radiative transfer equation (Magic et al. 2013):

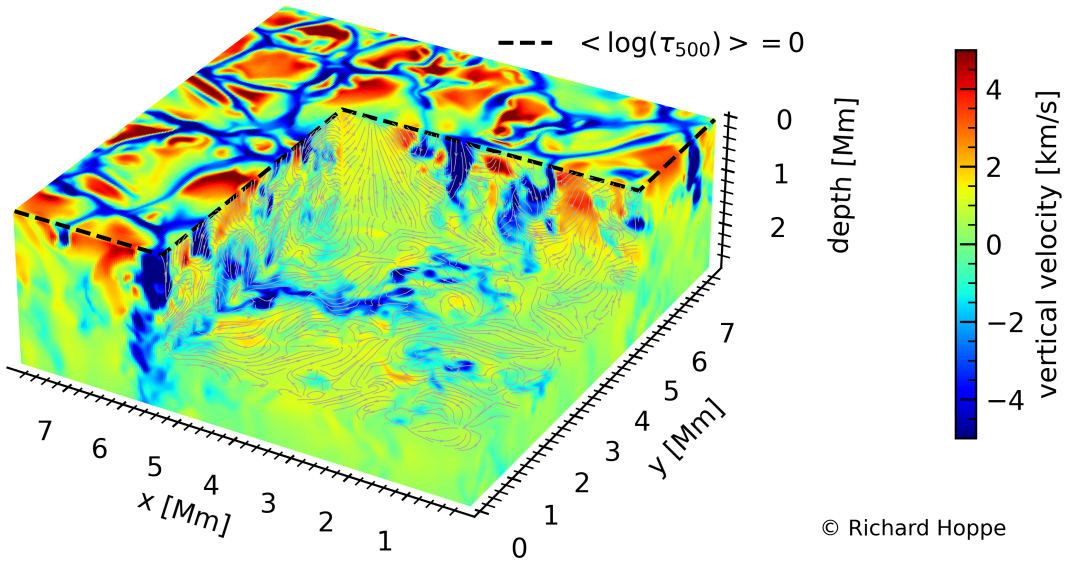

Figure 3: Snapshot of STAGGER model atmosphere showing the distribution of vertical velocity. The upper bound is the optical depth where $\log\tau_{500} \approx 0$. Reproduced with permission from Bergemann et al. (2021).

$$Q_{\rm rad} = 4\pi\rho \int_\nu \kappa_\nu (J_\nu - S_\nu)\, d\nu \tag{44}$$

and $Q_{\rm visc}$ is the viscous dissipation

$$Q_{\rm visc} = \sum_{ij} \tau_{ij} \frac{\partial v_i}{\partial x_j} \tag{45}$$

In the equations above, ρ is the mass density, $\boldsymbol{v}$ is the velocity field, $\tau_{\rm visc}$ is the viscous stress tensor, P is the thermodynamic pressure, g is the acceleration due to gravity, ϵ is the internal energy per unit volume, κ_λ the opacity specific to wavelength λ, S_λ the source function, and J_λ is

the mean specific intensity averaged over the total solid angle.

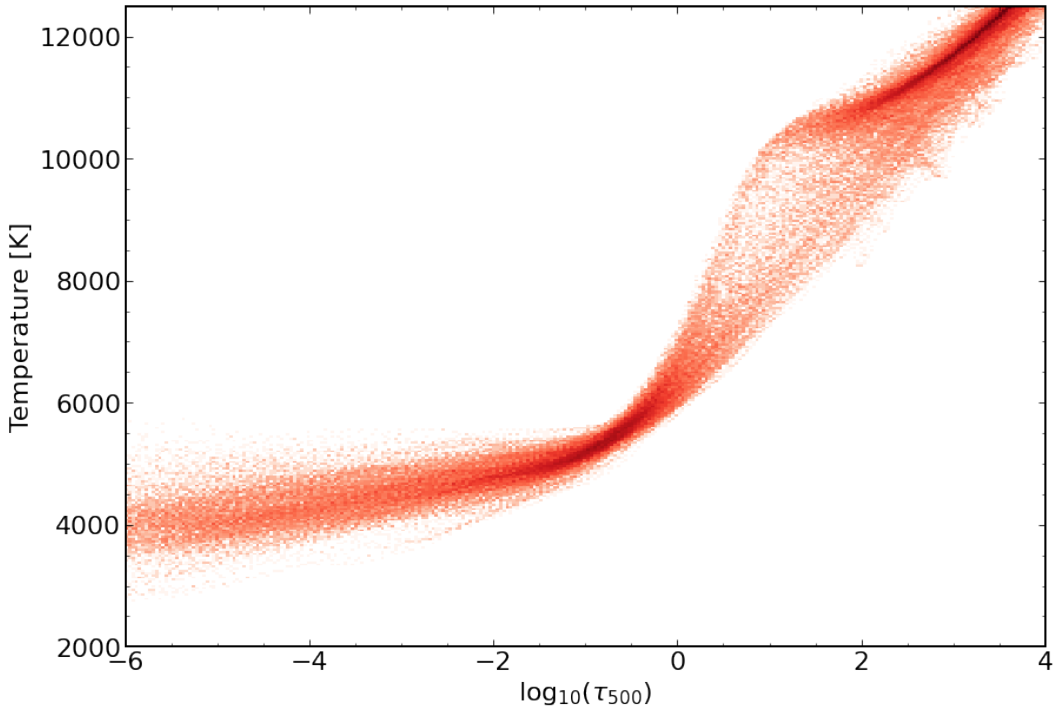

Figure 4: Histogram of temperature structure of the 3D STAGGER atmosphere snapshot, against the logarithm of optical depth of the material at 500nm.

4 Observational Data

We use observations of the Sun provided by Schäfer et al. (2020) as part of their solar flux atlas, taken at the Institut für Astrophysik, Göttingen (IAG) using a 50cm siderostat with a Vertical Vacuum Telescope and Fourier Transform Spectrograph (FTS). The FTS has a very high resolving power of up to R = 925,000 at 6000Å while taking solar observations in its double-sided mode. The observation apparatus incorporates a Laser Frequency Comb which ensures high precision and accurate frequency calibration (< 10 cm/s).

In order to investigate the centre-to-limb variation of calculated abundance, we require that the observed spectrum be spatially resolved, that is, we have an individual spectrum which corresponds to each contour on the solar disc representing angular distance from the centre of the disc (Fig. 6). We can consider θ, the angle with which radiation is emitted from the solar surface, relative to the normal of the surface. By convention we use the cosine of this angle, $\cos\theta \equiv \mu$, where $\mu = 1$ refers to radiation emitted from the centre of the solar disc $\mu = 0$ as the very edge, or limb.

Many individual spectra were recorded on quiet regions of the Sun for ~10 minutes each, then co-added, after correcting for barycentric motion and solar rotation. This enabled the combinations of observations of the same μ-angle. The spectra used in this study correspond to solar observations at μ-angles: 1.0, 0.9, 0.8, 0.6, 0.4, and 0.2 (Fig. 6), and cover the wavelength range 5500Å - 7100Å. Of the eight Si lines included in this range, two were not available due to telluric contamination. The processing of the remaining diagnostic lines is described in successive sections.

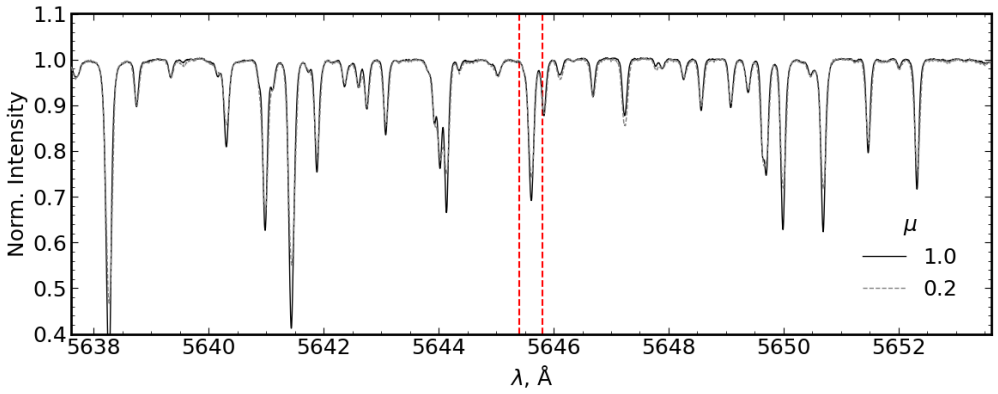

Figure 5: A section of the IAG spectra corresponding to observational angles $\mu = 1$ and $\mu = 0.2$, centred around the first diagnostic silicon line at 5645Å, highlighted in red.

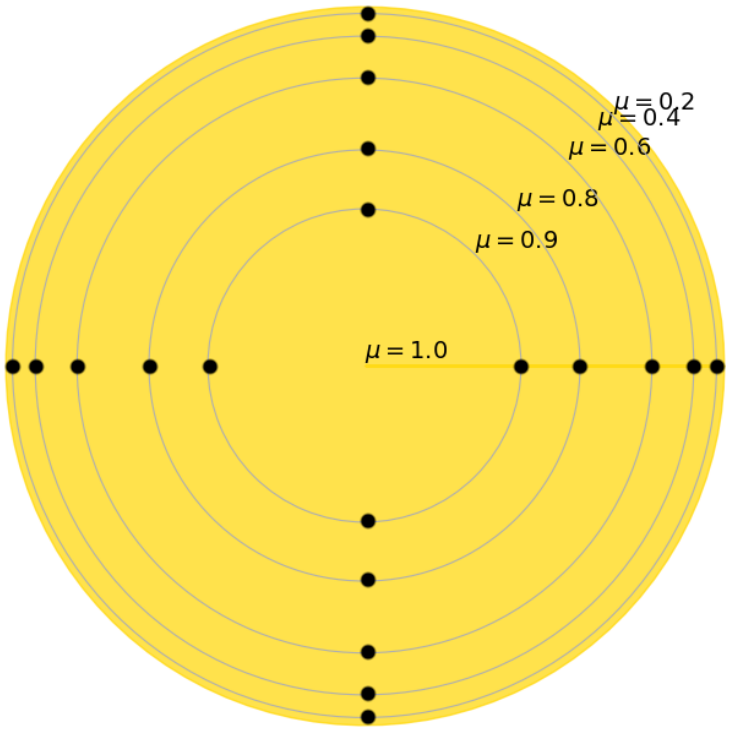

Figure 6: Representation of the μ angle on the solar sphere used in the centre-to-limb analysis. The 4 nodes per contour represent the coordinates of the corresponding modelled spectra.

5 Atomic model

The atomic silicon model used in this study is largely the same as that presented by Bergemann et al. (2013), more recently updated (Magg et al. 2022). It comprises values for the excitation energy and statistical weight corresponding to 289 Si I, and 49 Si II ionisation energy levels. It incorporates fine structure splitting in the levels with energies lower than 7.45eV and 6.2eV for Si I and Si II levels, respectively.

For the spectral lines, the model includes information on the corresponding transition levels, the *f-values* (oscillator strengths), and the damping constants: GA, the inverse lifetime of the upper level, GVW the van der Waals broadening parameter, and GS the Starck broadening parameter.

The model covers 2826 Si I transitions sourced from the NIST database (Kramida et al. 2019) and Kurucz database (Kurucz 2016), and 130 Si II transitions, from NIST. Also detailed in the model atom are photo-ionisation cross-sections and rate coefficients for inelastic collisions taken from Belyaev et al. (2014).

The model atom includes the rate coefficients for a large number of transitions which result from bound-bound excitation transitions in neutral species mediated by free electrons, bound-bound transitions mediated by neutral hydrogen, bound-free ionisation transitions mediated by free electrons, and charge transfer with neutral hydrogen. For each transition the rate coefficient is specified for a range of temperatures.

In order to perform our abundance analysis, we focus on five of the strongest absorption lines in the silicon spectrum to use as diagnostic lines. These were further reduced to three lines, due to issues with processing the corresponding lines in the observed spectra. The parameters for the diagnostic lines are shown in Table 1. Two other strong lines, at 5793.073Å and 5690.425Å, were considered for analysis and are used in other similar studies (such as Amarsi & Asplund (2017)) but are omitted from this study due to gaps due to telluric contamination in the IAG ob-

served spectrum. In addition, we include the new oscillator strengths calculated by Rhodin et al. (2018), via a combination of theoretical lifetimes, and experimental branching fractions using their Fourier transform spectrometer at Lund University. Oscillator strengths from Kurucz (2016) and Rhodin et al. (2018) are used to calculate the Si abundance.

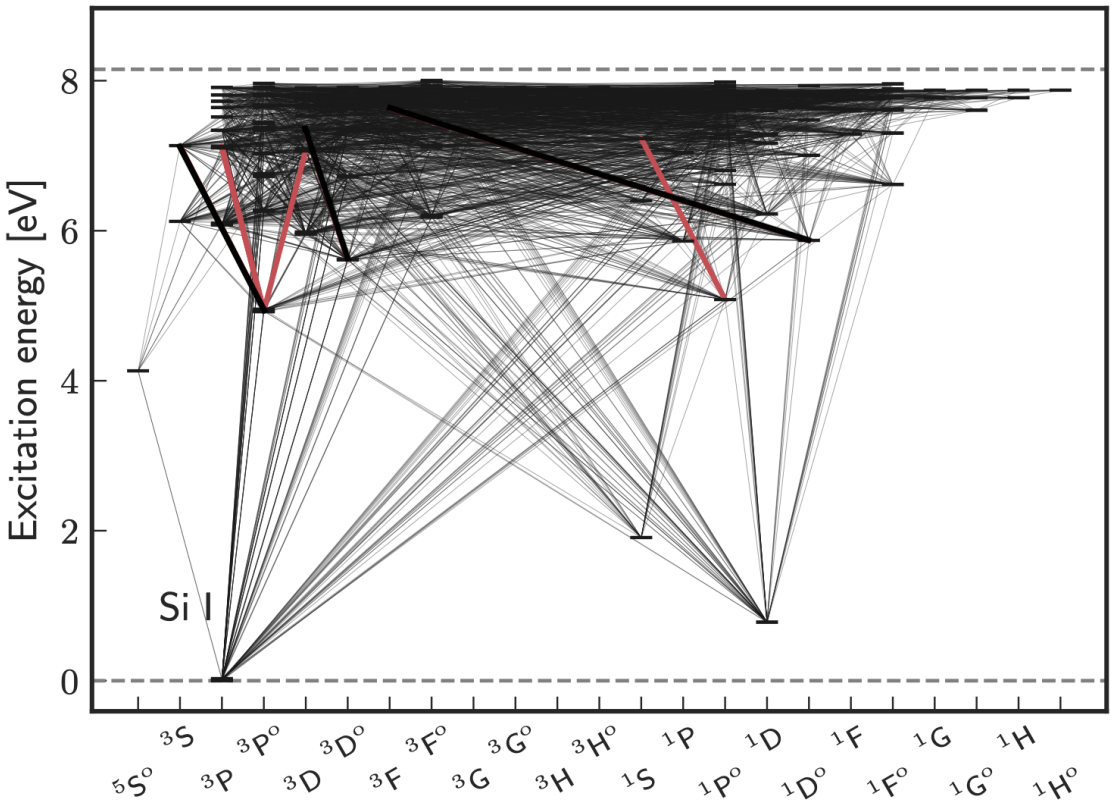

Figure 7: Grotrian diagram showing the energy levels of the model silicon atoms with the bound-bound transitions in black. Red lines correspond to the diagnostic absorption lines used in the abundance analysis. Reproduced with permission from Magg et al. (2022).

λ (Å)	E_{upper} (cm^{-1})	E_{lower} (cm^{-1})	g_{upper}	g_{lower}	log gf
5645.613	57468.238	39760.285	5	3	-2.140[1] -2.067[2]
5684.484	57541.918	39955.055	3	5	-1.420[1] -1.607[2]
5701.104	57295.883	39760.285	1	3	-2.050[1] -1.981[2]
5772.146	58311.660	40991.883	1	3	-1.750[1] -1.643[2]
7034.901	61563.305	47351.555	16	5	-3.714[1] -0.78[2]

Table 1: Atomic parameters for the diagnostic Si I lines from the model atom. We include the wavelength of the spectral line, the upper and lower energy levels of the transition corresponding to the line, g the statistical weight for these levels, and log gf where f is the oscillator strength. Source: [1] - Kurucz (2016), [2] - Rhodin et al. (2018).

6 Methods

With the model atmospheres produced by the Gustafsson et al. (2008) and Magic et al. (2013) groups, we simulate radiative transfer in the atmosphere with MULTI3D. These spectra were analysed to interpret the behaviour of the models, and to compare with the observed data, to calculate abundance estimates. In this methods section we outline the processes by which such calculations were made.

6.1 Calculation of equivalent widths

The equivalent width (EW) is one of the characteristics of a spectral line designed to describe its 'strength', without requiring knowledge or explanation of its detailed shape, and is our primary metric for comparison of the different synthesised spectra and of these with the observed spectra. The width in question is that of the rectangle along the wavelength axis, which is formed with equal area to the spectral line relative to its adjacent continuum, and with height equal to the level of continuum intensity measured from a zero intensity. The equivalent width rectangle and its spectral line absorb the same volume of photon flux. This width can be defined symbolically as:

$$W_\lambda = \int \frac{(I_c - I_s)}{I_c} d\lambda \tag{46}$$

with I the intensity at c, the continuum; and s, the spectral combination of both the line and the continuum. A graphical representation can be seen in Fig. 8. The EW serves as a useful measure of spectral feature strength, as it is not sensitive to the effects of phenomena which may change the shape of the line, such as Doppler broadening (Collins et al. 1989).

In practice, the EW of each of our diagnostic spectral lines was calculated by selecting a point on either side of the normalised peak, where the line intensity returns to the continuum, and finding the area between the peak and the continuum, bounded by these points, with Simpson's

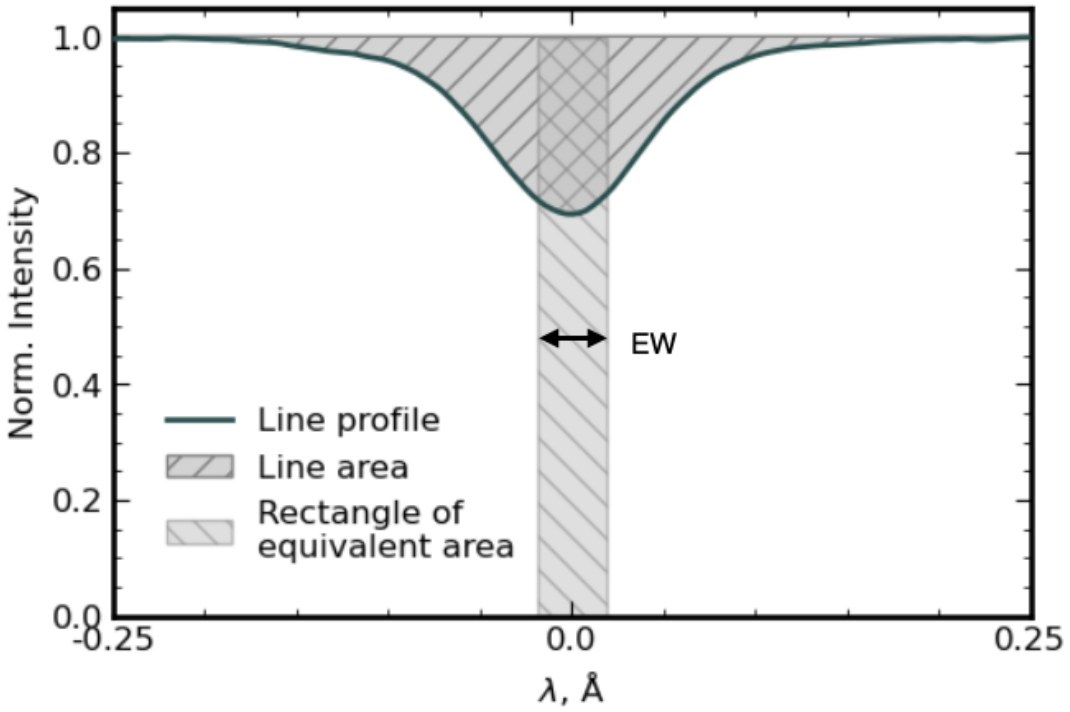

Figure 8: Diagram explaining the equivalent width of a spectra line.

integration method. The width can then be found using this area in each case using the procedure detailed above.

6.2 Observed spectrum processing

The observational data is made up of a normalised intensity spectrum spanning the frequency range covered by our diagnostic lines for each of the 6 μ observation angles which were syntheised by MULTI3D. For each diagnostic line we then attempt to isolate the corresponding peak by choosing the limits of its wings, where we consider the intensity to return to the continuum value. This is made difficult by the presence of contaminating spectral lines which form at wavelengths close to that of the diagnostic line and thus overlap to some degree with the line of interest. We call these lines 'blended', and as the neighbouring lines are usually correlate to different atomic transitions, to that of the diagnostic lines, they are not relevant to the analysis, and must be removed.

To de-blend a diagnostic line, we take representations of line features in the form of Voigt profiles. We therefore make a fit with a non-linear least-squares optimiser, with σ, the standard deviation of the Gaussian part, and γ, the half-width at half-maximum (HWHM) of the Lorentzian part, as free parameters. The contaminating features are thus fitted as Voigt profiles, and these are masked from the processed spectra, leaving an approximation the desired spectral line as if it was formed without the presence of the contaminants.

For example, we show the deblending of line at 5645.6Å due to a smaller line at 5645.8Å in Fig. 9. Deblending is performed at the required lines for each μ angle spectrum.

Subsequently, the intensities corresponding to each line are normalised to the continuum intensity, using the limits discussed above. The resulting renormalised line is shown in the lower panel of Fig. 9. In this situation there is very little difference before and after renormalisation, however this is not the case for each of the other lines.

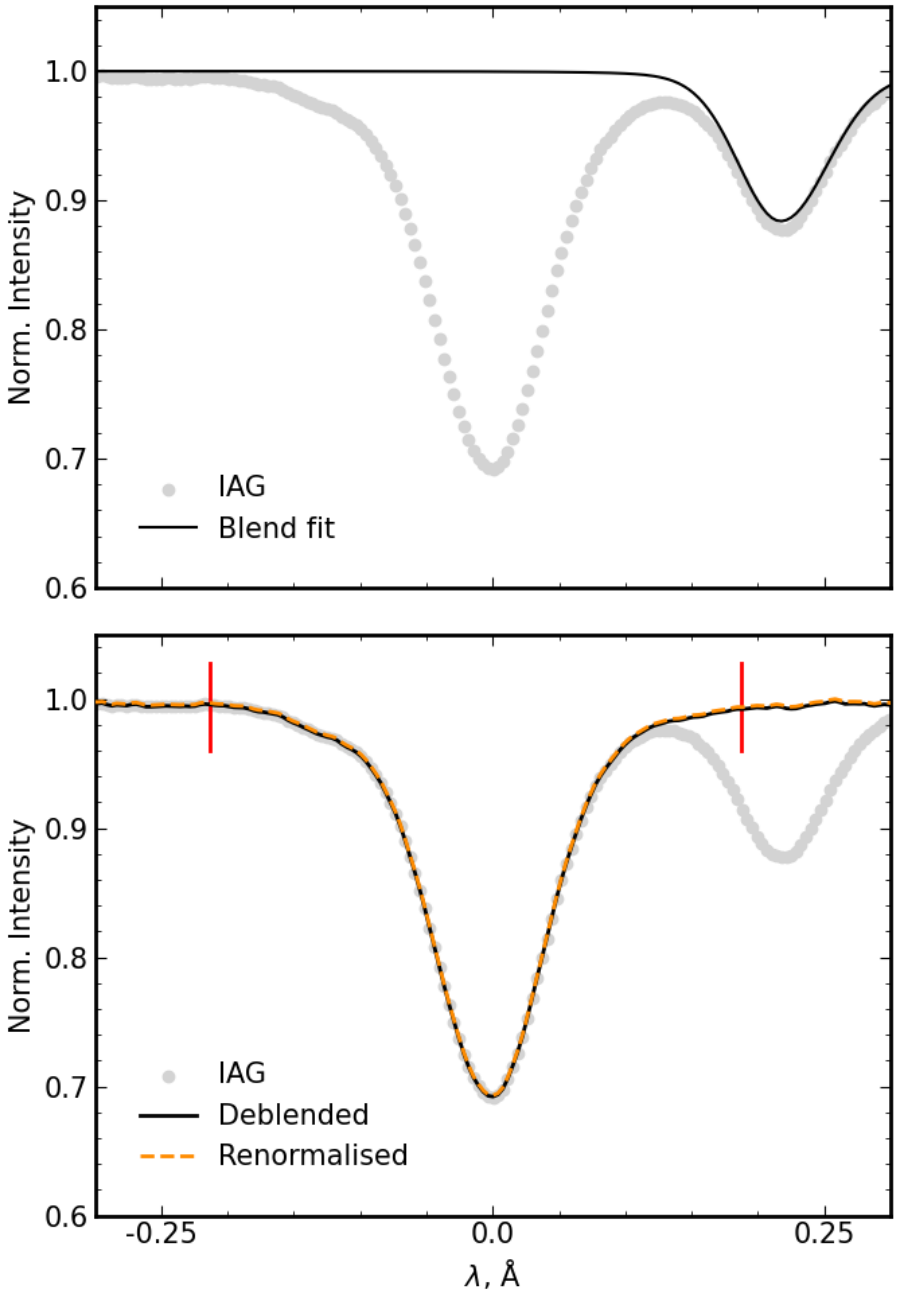

Figure 9: Top: Observed profile of silicon diagnostic line at 5645Å in the $\mu = 1$, and the fit to the neighbouring smaller line. Bottom: Profiles with the blend removed, and subsequently renormalised to the continuum. The vertical lines denote the limits of the line, where the continuum normalisation is applied.

6.3 Abundance Differences and Abundance Calculations

The method by which we compare the observed spectra and computationally synthesised spectra is known as the curve of growth (CoG). This involves forming a relationship, corresponding to each μ angle and each diagnostic line, which describes the change in EW as the relative abundance of the chemical species in question is changed. Essentially, this is a fitting of the model to the observed data with the *curve*, which is this relationship of EW vs chemical abundance.

As 1D LTE simulations are typically much faster to compute than 3D non-LTE simulations, it is common to build the array of simulated values with differing abundance, to which the data must be fitted, with these 1D LTE simulations. However, we wish to use 3D non-LTE simulated spectra for comparison with the observed data, as this is assumed to be most accurate. We resolve this with the well established method of using *abundance differences*, commonly called *abundance corrections*, which describe the difference in abundance between that calculated with a particular 3D non-LTE line, and that corresponding to a line produced with a different simulation method. It is well established that that this abundance difference procedure is an accurate and robust way of inferring the calculated abundance corresponding to a 3D non-LTE line, without requiring the expensive simulation of a 3D non-LTE CoG.

In practice, we use a range of 9 relative solar silicon abundances evenly spaced between 7.36 and 7.76 dex, and synthesise spectra under 1D LTE conditions for each abundance. For a given Si line and μ, the EW corresponding to each 1D LTE simulation is then calculated. We then approximate the EW-relative abundance relationship with a quadratic interpolation using the CoG points. This is used to estimate the relative abundance of a 1D LTE simulation with the same EW as that of the 3D non-LTE simulated line. The abundance difference in each case is thus the difference between this interpolated abundance and the initial abundance used to simulate the 3D non-LTE spectrum, 7.56 dex.

To find the estimated relative abundance of the observed spectra, we

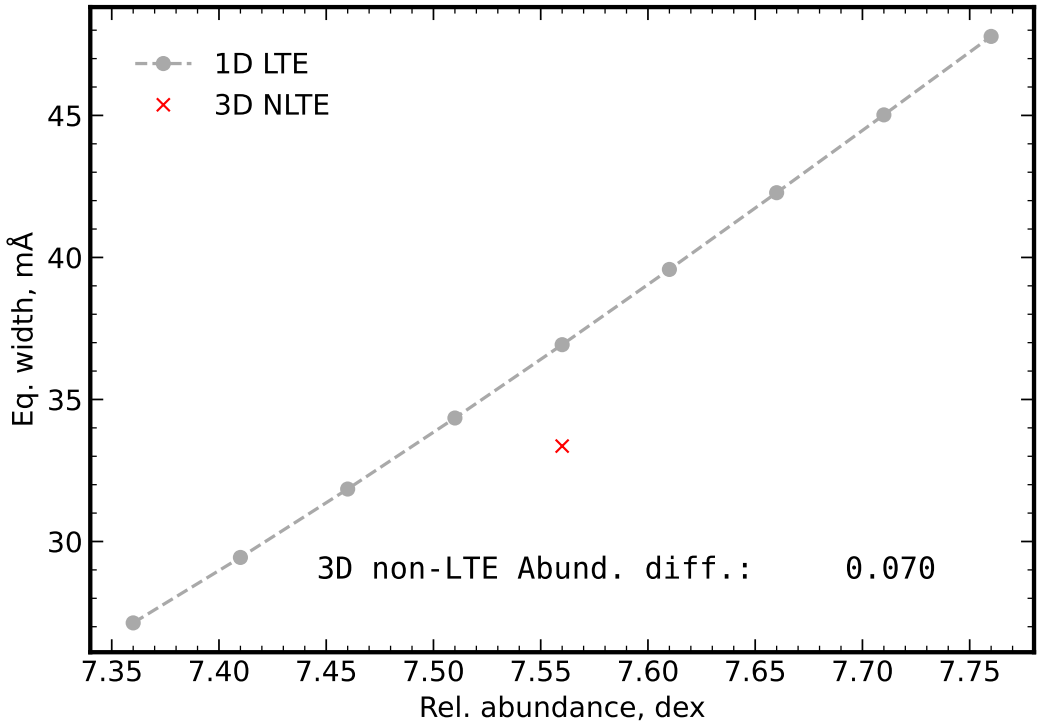

Figure 10: Abundance Difference example for the 3D non-LTE simulations for the 5645Å line.

now compare these lines with those of the 1D LTE synthesised spectra. We use the array of 1D LTE simulated spectral lines, with different relative abundance of silicon, to again interpolate to find a relationship between the EW and relative abundance of the 1D LTE CoG, and thus estimate the relative abundance of each of the lines of the observed spectrum. We now apply the 3D non-LTE abundance differences (or 1D non-LTE / 3D LTE differences) to these 1D LTE relative abundances, to find a more accurate approximation of the silicon abundance corresponding to the observed solar spectral lines. In this study we calculate the estimated abundances for 1D non-LTE, 3D LTE and 3D non-LTE, which permits us to compare the performance of each model.

7 Results

7.1 Comparative analysis of 1D non-LTE and 3D non-LTE abundance differences

Shown in Tables 2, 3 and 4 are the calculated centre-to-limb abundance differences for the 1D non-LTE , 3D LTE and 3D non-LTE simulations, respectively, in dex. The abundance differences refer to the difference in relative abundance of the 1D LTE curve of growth at the equivalent width of the other simulations at the starting abundance for each line, μ pair. Therefore, according to the calculations in this study, a negative abundance difference denotes a case where the equivalent width of the line is greater in the corrected calculation than in 1D LTE, while for a positive abundance difference the reverse is true.

μ	Line λ (Å)		
	5645.613	5772.146	7034.901
1.0	0.019	0.018	0.014
0.9	0.018	0.017	0.013
0.8	0.017	0.015	0.011
0.6	0.012	0.009	0.004
0.4	0.000	-0.007	-0.011
0.2	-0.049	-0.068	-0.060

Table 2: Abundance differences for 1D non-LTE.

In Fig. 11 we plot the abundance difference relationship with μ for the 1D and 3D non-LTE simulations, for the line at 5645.61Å. In both cases the abundance difference becomes more negative as we move from

μ	Line λ (Å)		
	5645.613	5772.146	7034.901
1.0	0.045	0.045	0.063
0.9	0.026	0.013	0.008
0.8	0.026	0.013	0.010
0.6	0.009	-0.009	-0.023
0.4	-0.034	-0.061	-0.083
0.2	-0.117	-0.155	-0.178

Table 3: Abundance differences for 3D LTE.

the disc centre to the limb, with this appearing more pronounced in the 3D non-LTE case. The difference in line strength can be seen in Fig. 12. Here it is shown that there is a large weakening of the 1D non-LTE line between the disc centre ($\mu = 1$) and the limb ($\mu = 0.2$). Relative to the 1D LTE line, the 3D non-LTE line is weaker in the centre and stronger in the limb, which is the reverse of the 1D non-LTE line's behaviour. This follows the trend that is shown in Fig. 11.

In each of the diagnostic lines there are positive abundance differences at the disc centre, and negative differences at the limb, with the transition falling somewhere between $\mu = 0.8$ and $\mu = 0.2$. If we compare 1D non-LTE and 3D non-LTE at each line and μ (Tables 2 and 4), then in 3D non-LTE we see a more negative abundance difference at every individual point.

Taking the line in Fig. 12 as an illustrative example, one can see the cause of the large negative 3D non-LTE abundance difference at the limb by comparing the EWs. Relative to the 1D LTE line, the 3D non-LTE line is significantly stronger at the limb, and somewhat weaker in the disc

μ	Line λ (Å)		
	5645.613	5772.146	7034.901
1.0	0.070	0.068	0.081
0.9	0.051	0.036	0.026
0.8	0.049	0.034	0.025
0.6	0.026	0.004	-0.016
0.4	-0.031	-0.067	-0.095
0.2	-0.171	-0.233	-0.247

Table 4: Abundance differences 3D non-LTE.

centre. The 1D non-LTE behaviour mirrors this trend, but to a smaller degree - reflected in the less steep change in abundance difference seen in Fig. 11.

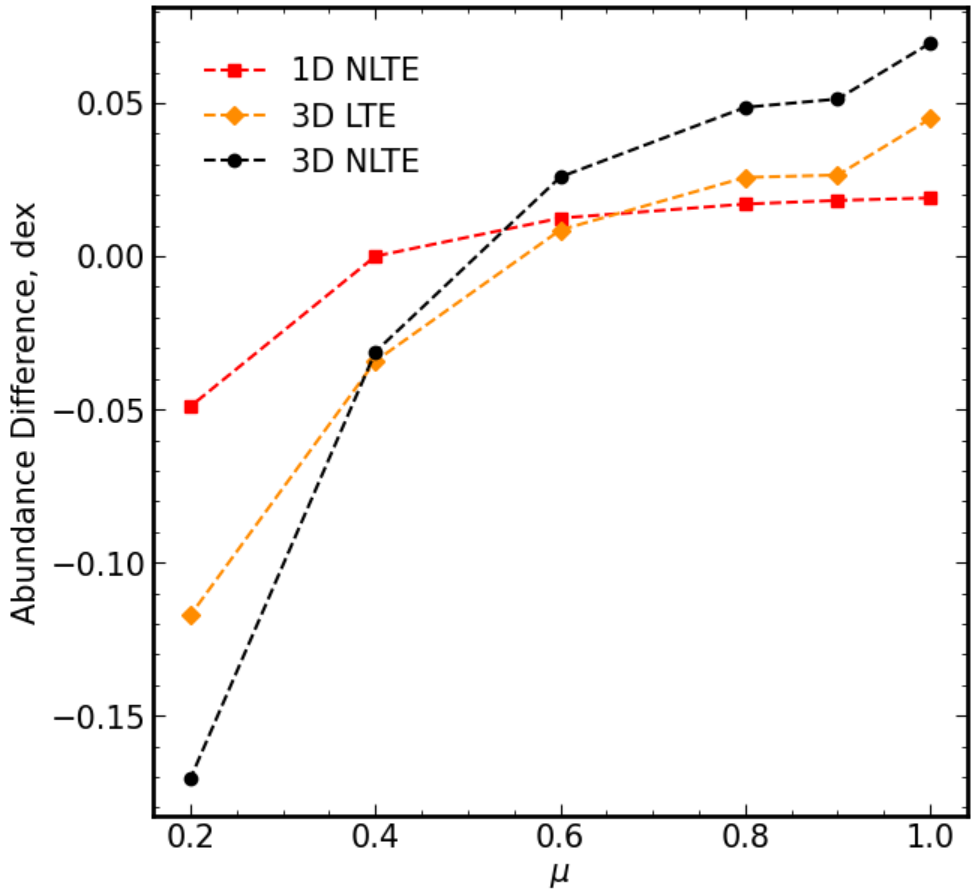

Figure 11: Centre-to-limb Abundance Differences for the 1D and 3D non-LTE simulations for the 5645Å line

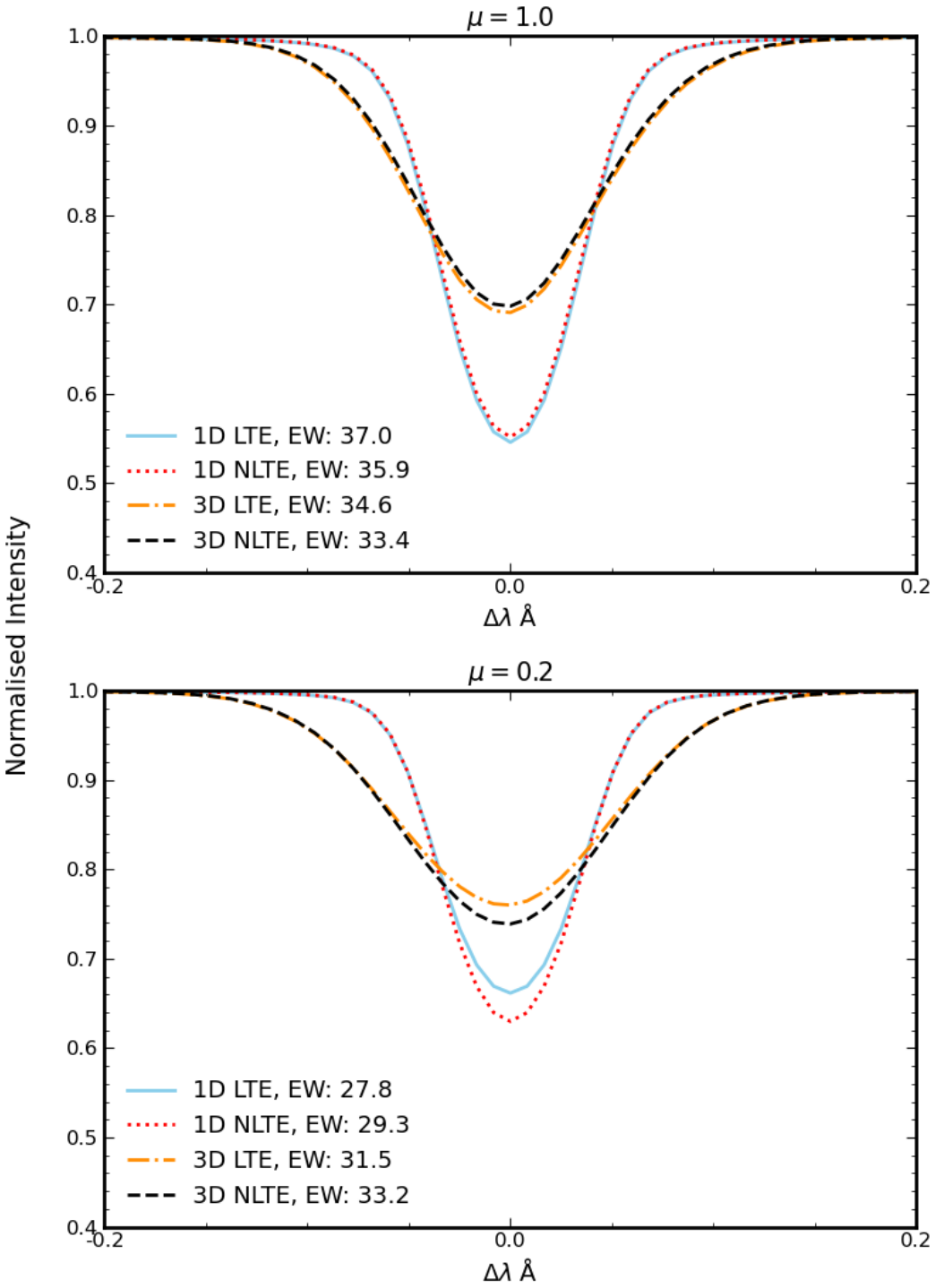

Figure 12: Normalised line profiles at the disc centre and limb for the 1D LTE, 1D non-LTE, and 3D non-LTE simulations for the 5645Å line. Equivalent widths are given in mÅ.

7.1.1 Centre-limb comparison of lines in 1D LTE

In order to explain the difference in equivalent widths of the 1D LTE line between the disc centre and the limb, we must consider both the influence of the line formation at each angle, and the difference in the continuum across the disc. By plotting the unnormalised intensity profiles of the line at 5645Å (Fig. 13) it can be seen that there is a significantly lower continuum intensity at the limb than at the disc centre in the spectrum synthesised by MULTI3D.

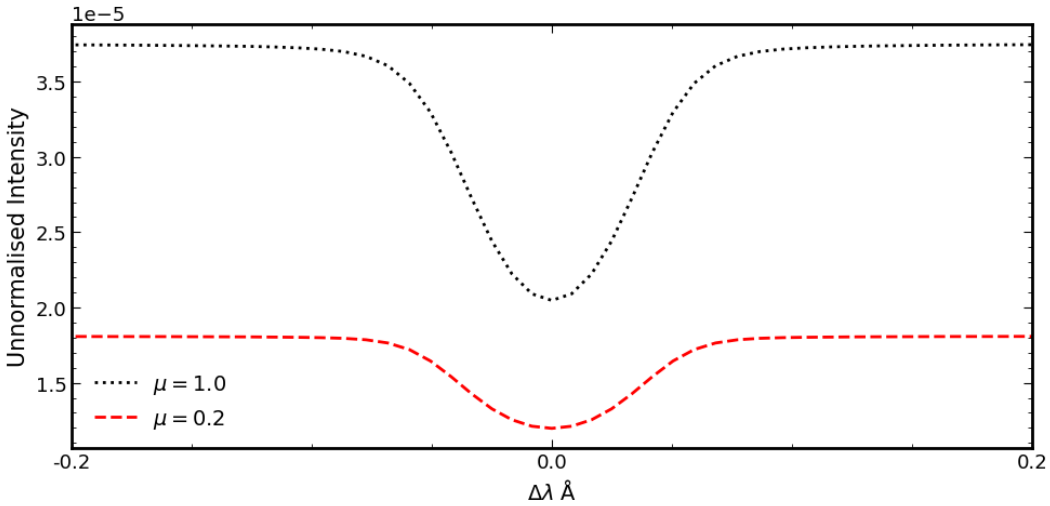

Figure 13: Unnormalised line profiles at the disc centre and limb for the 1D LTE simulations for the 5645Å line, with intensity units erg $cm^{-2}s^{-1}Hz^{-1}\Omega^{-1}10^{-5}$.

The cause of this difference in continuum intensities is due to the geometry of the atmosphere and the difference in the path which the vertical rays and inclined rays follow. As the models discussed in this study are plane parallel atmospheres, we extend the 1D model by building a heterogeneous 2D 'slab' at each depth point (Fig. 14). One may view the temperature structure experienced by an angled ray by tracing a line along a μ angle, beginning from an arbitrary location on the surface of the atmosphere, and interpolating the temperature at regular intervals along the line. For $\mu = 1$ this is simply the temperature along a vertical 1D

column, but for $\mu = 0.2$ the geometry of the simulated box means that the line exits from the side of the 'slab' before reaching the bottom, requiring that periodic boundary conditions are used to re-enter the 'slab' from the opposite boundary.

The two paths traverse the same vertical temperature gradient (dz) in the box, but the distance covered by the rays differs; the inclined path, corresponding to $\mu = 0.2$, covers a distance $\sim$ 5x larger than the vertical path, in real space.

In general, the difference in path length in a plane parallel atmosphere, which corresponds to different μ may be expressed by calculating the the optical depth, and is given by

$$d\tau_\mu = \frac{d\tau_{\mu=1}}{\mu} \tag{47}$$

meaning that the ratio of optical depth corresponding to an emergent angle θ relative to the vertical direction is simply $1/\mu$ (see Fig. 14).

One may extend this geometrical approach (such as by Sánchez-Bajo et al. (2002)) to arrive at a limb-darkening law, such as:

$$I_\lambda(\mu) = I_\lambda(0)\left[1 - u_\lambda(1-\mu)\right] \tag{48}$$

where a linear source function leads to a description of the intensity along an emergent angle θ and u_λ, a limb darkening coefficient.

It is also instructive to consider the temperature profiles corresponding to the optical depth in the simulated space. For this we choose the optical depth at a so-called *standard* wavelength at 500nm, which is situated in the visual range and is fairly representative of the the optical depth of the stellar continuum. Seen in Fig. 15, these profiles show that there is a marked difference in the temperature structure along the geometrical paths corresponding to these two lines of sight. At the position along the line of sight in the $\mu = 0.2$ case where the medium becomes optically thin ($\tau = 1$, or $\log(\tau) = 0$), the temperature change is very rapid over optical depth, and here the temperature is $\sim$2000K lower than its counterpart in the disc centre.

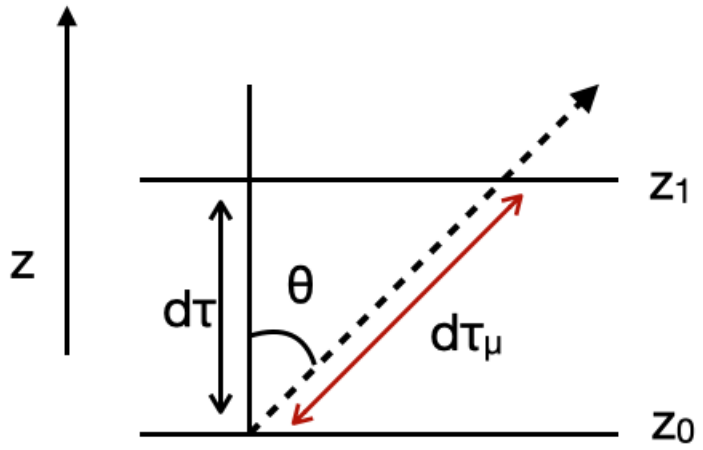

Figure 14: Diagram of a plane parallel atmosphere which shows a line of sight through the atmosphere inclined to the vertical at an angle of θ, and illustrates the difference in optical depth along the vertical ($d\tau$) and inclined ($d\tau_\mu$) paths, over the same period of radial depth (dz).

In LTE we expect the Planck function to describe the intensity of the material similar to that of a blackbody, defined by its frequency and temperature, as in Equation 10. With the temperature disparity shown in Fig. 15 and the Planck equation, we see the explanation for the difference seen in continuum intensity in Fig. 13.

It must be remembered that the effects discussed above are not artefacts of the 1D model atmosphere, but instead a physical phenomenon present in the Sun, and reproduced by any simulation with this geometry. Situations in which a photon remains for longer in the medium before escaping from the solar surface suggest a higher probability of the photon being absorbed by the continuum. At the limb the longer path distance induces this longer travel time, in turn suggesting a lower photon flux, a pattern observed at the limb.

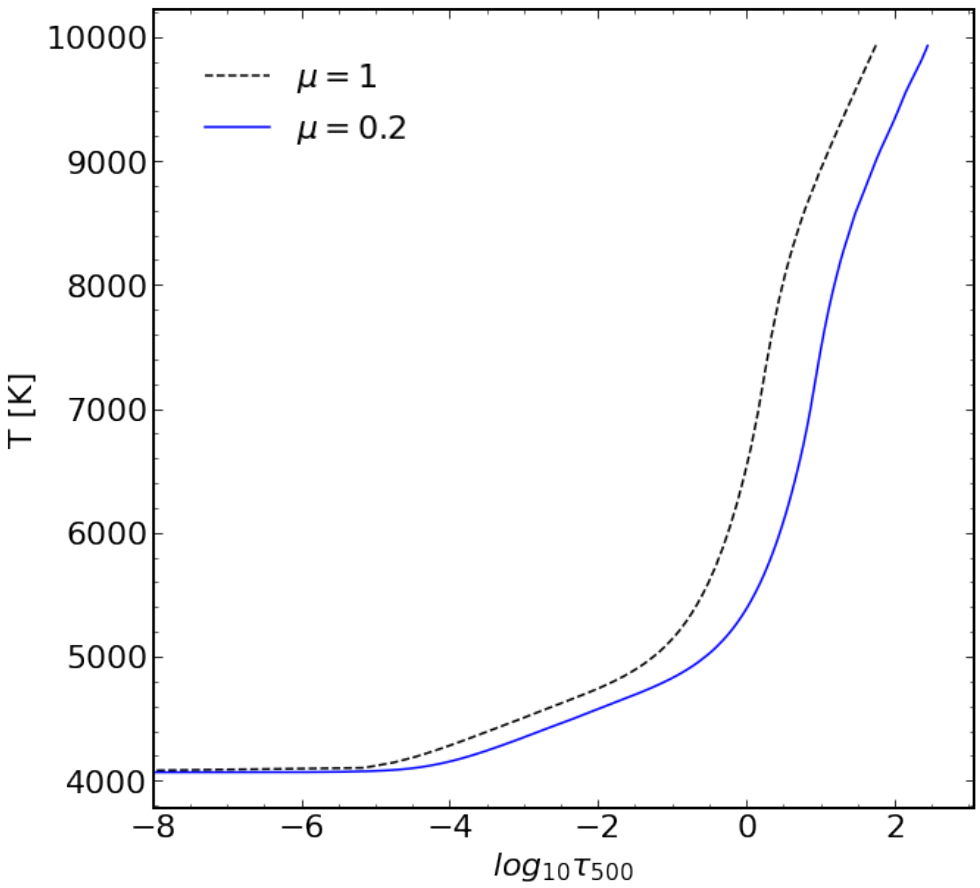

Figure 15: Horizontally averaged temperature structure of the 1D MARCS model atmospheres, corresponding to the logarithm of optical depth at 5000Å at both the limb and disc centre. The structure is shown for both the centre and limb viewing angle paths. The optical depth in this figure is calculated for the specific path geometry, as τ_μ in Equation 47.

7.1.2 Centre-limb comparison of 3D lines

Referring back to Figs. 11 and Fig. 12, we see the distribution of the the abundance differences and equivalent width for an example diagnostic line, from the centre-to-limb. We saw that for lines synthesised in non-LTE in the STAGGER 3D model atmosphere, there is very little difference in equivalent width across the limb, meaning that we see significant abundance differences due to the large change in EW across the limb for the 1D LTE lines, as explained in the preceding subsection. For the 3D LTE synthesised line, we see a smaller change in EW than that of the 1D lines, yet still larger than that produced in 3D non-LTE. (Figs. 16).

When calculating emergent intensities in 3D, MULTI3D traces multiple 'rays' through the simulation volume from the bottom to the top, along the μ angles specified. At each depth point (ie. at the vertical depths which have layers of grid points), the radiative transfer equation is solved using physical parameters which are interpolated based on the local grid points. As μ decreases from 1, the longer path length due to the geometry described earlier also applies, meaning that we should expect to see lower EW at lower μ. In contrast to the simulations that use the 1D MARCS model, we now also consider the influence of convection in the 3D STAGGER model.

Fig. 17 shows the temperature profile with depth of the 3D STAGGER model atmosphere snapshot which we have used for the analysis in this work. For the vertical ray ($\mu = 1$), there is a steep increase of temperature with depth, as seen in the 1D model. However, at the limb, we see a markedly different pattern to that seen in the 1D model, with a significantly less smooth increase in temperature, and instead a modulated trend, with even non-monotonic behaviour at smaller scales. We attribute this behaviour to the convection cells, which feature regions of alternating hot and cold regions in the horizontal axis (discussed further in the next section). As a ray is traced though a series of these cells, it experiences a variation in the local effective temperature, causing an effective averaging of temperature with depth due to the mixing of matter in the atmosphere.

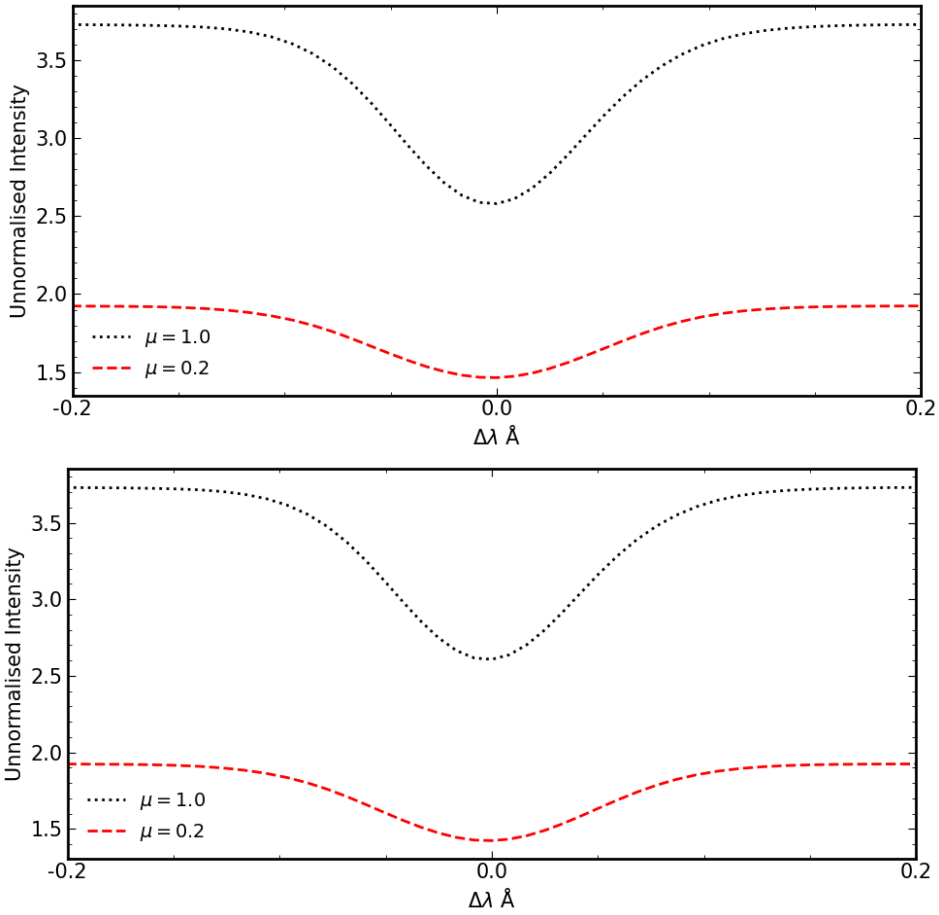

Figure 16: Unnormalised line profiles at the disc centre and limb for the 3D LTE (top) and 3D non-LTE (bottom) simulations for the 5645Å line, with intensity units erg $cm^{-2}s^{-1}Hz^{-1}\Omega^{-1}10^{-5}$.

We thus assume that the lesser difference in EW across the limb in 3D, as compared to 1D, is due to the effect of the convection cells to push the temperature profile of the inclined ray closer to that of the vertical ray. The effect of this non linear behaviour is difficult to explain, as the consequences of this modulated temperature and density profile are combined with the non-linear radiative transfer dynamics, creating a very complex situation.

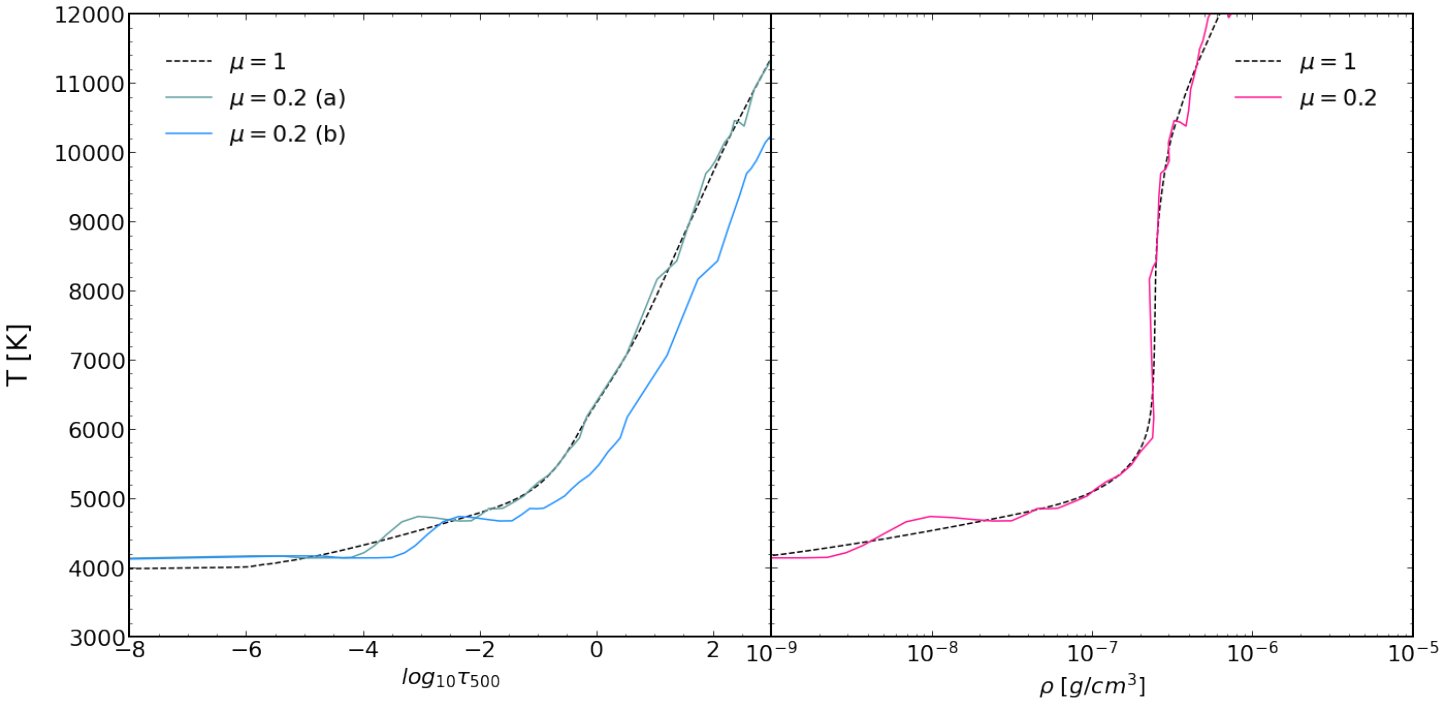

Figure 17: Horizontally averaged temperature (left) and density (right) profiles of the 3D STAGGER model atmosphere. In the left-hand plot the inclined ray labelled (a) shows the vertical optical depth, this is, the optical depth through which the inclined 'ray' passes defined for a vertical path. The line labelled (b) shows the specific optical depth along the inclined ray, such as τ_μ in Equation 47.

7.2 Waveshift and asymmetry of the line profiles

The waveshift of a spectral line and its asymmetry are evidence of 3D effects in the line formation medium, and can be illustrated by using the method of line bisectors. These are formed by finding the midpoint wavelength of the line profile across its depth. These midpoints are plotted, and the resulting line shows the bisector of the profile. In practice, this was performed by fitting cubic splines to the intensity data points of the lines, and finding midpoints of the intersections between the fit and a series of horizontal lines spanning the intensity range. Bisectors have been widely used to investigate the effect of stellar parameters on line structure, such as effective temperature and luminosity (Gray 2005), and on centre-to-limb variation on line profiles (Dravins & Nordlund 1990).

Figure 18 illustrates the line asymmetries in the 1D LTE, 3D non-LTE, and 3D LTE simulated lines at 5645.61Å, and the observed line from the IAG spectrum at the same wavelength, all normalised to the continuum intensity. Again we can compare the behaviour at the solar disc centre to that that the limb, and see the behaviour due to the different models.

Line asymmetries are present in the 3D simulations, but not the the 1D simulations, which was expected, due to the lack of convection in the 1D MARCS models. This can be seen by the lack of any Dopper shifts in the 1D LTE plot, and the curvature in the others. In panel (b) of Fig. 18 it can be seen that in 3D non-LTE there is in general limited asymmetry, but convective blueshift is present, and blueshifting increases from the centre to the limb, with the exception of the behaviour of the $\mu = 0.2$ bisector. This line appears to be less blueshifted than expected along its length, but with higher blueshifting at the line's maximum than at its minimum (peak) which is the reverse of the trend seen in the other bisectors.

Asymmetry is also present in the observed spectrum (Fig. 18 (d), and we see again convective blueshift for $\mu = 1$ to $\mu = 0.4$, but we see a less well defined trend of blueshifting from the centre to the limb as that

produced by the 3D non-LTE simulations. Again, the $\mu = 0.2$ bisector exhibits more distinct behaviour with a red shift of ~200m/s relative to the bisectors from the rest of the disc. There is more slightly more pronounced asymmetry here; with a shift of ~ 200m/s along the depth of the line.

The reason for the presence of asymmetry in the line profiles of the 3D synthesised and observed spectra is that in 3D STAGGER atmospheres exhibit convection, a phenomena emergent from the equations of time-dependent hydrodynamics, and present in the real Sun. Convection can

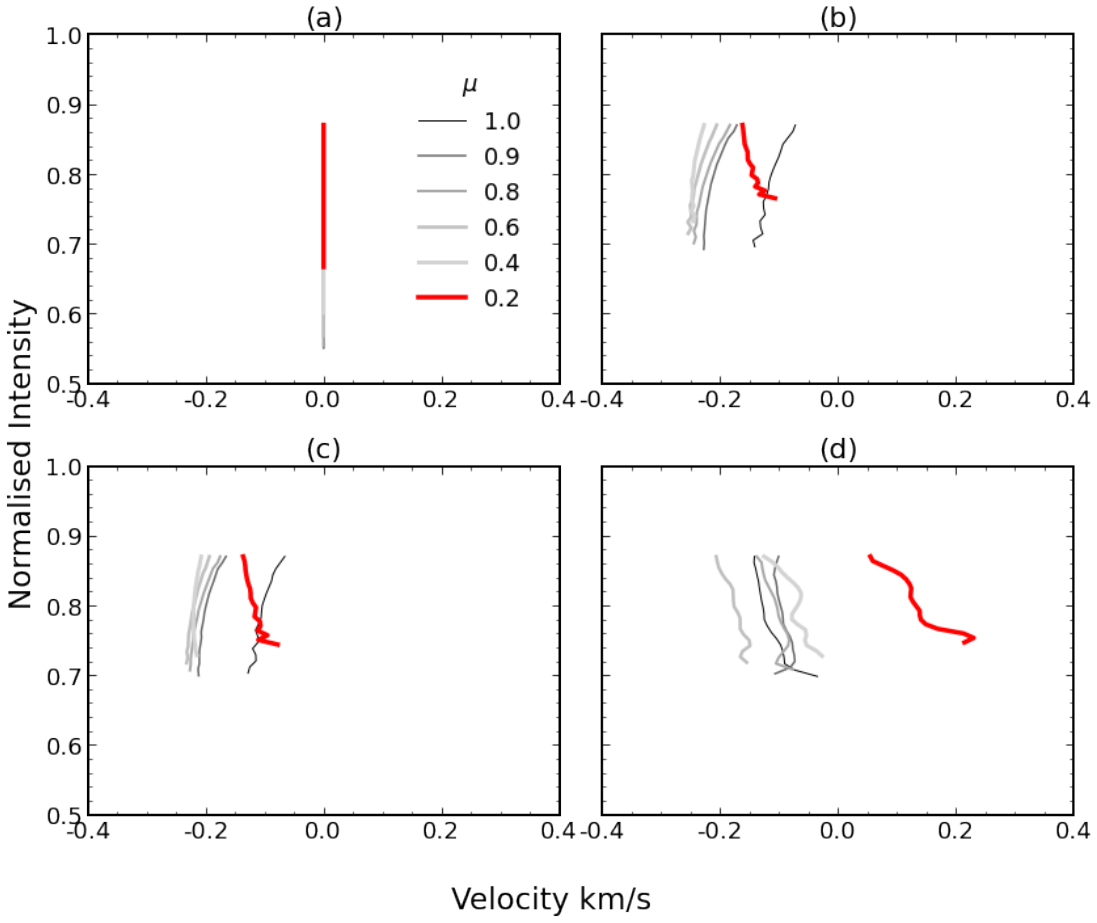

Figure 18: Bisectors of line profiles at 5645Å, for each μ. (a) 1D LTE, (b) 3D non-LTE, (c) 3D LTE, (d) IAG spectrum.

be considered a type of macroturbulence, involving movement of matter in an area larger than the formation regions, in contrast to microturbulence which takes place over a smaller region. The influence on the line profiles is explained by, taking in the first case of the normal line of sight, the movement of stellar matter in a convective cell towards and away from the observer. This convective velocity produces a Doppler broadening effect, shifting the line to higher frequencies for oncoming matter and lower frequencies for receding matter. The strength of the lines is not affected by convection velocity, as each line is entirely formed inside regions of comoving matter (Emerson 1998). Instead, the total effect is of the combination of many such regions, with different velocities in different convection cells contributing to a single line.

In the Sun, we are able to observe so-called granules, seen in Fig. 19, which exhibit dark granular lines of cooler falling matter surrounding bright central granules of rising matter. Thus, we have in this picture regions of receding, red Doppler shifted matter which is also cooler and thus dimmer, and the opposite regions of hotter, rising, blue shifted matter. The asymmetric nature here stems from the difference in line formation at different temperatures. The microphysical effects detailed earlier, which give rise to, and control the strength of spectral lines, are dependent on this temperature. In the case of silicon, the lines are strengthened at higher temperature, meaning that the blue shifted radiation from rising regions contributes more to the composite line than the weaker, falling element. Moreover, effects such as ionisation and excitation do not have a linear variation with temperature, leading to non-linear effects, and asymmetric behaviour in the line profiles.

Emerson (1998) argue that there ought to be a lesser degree of asymmetry at the limb, due to the orientation of the convection cells. The matter in the cells always rotate as approximate rectangles with rounded corners, with the rising and falling velocities parallel to the star's radius. As the line of sight moves from the centre of the star toward the limb, the component parallel to the rising/falling velocity falls, until, at the very limb, the line of sight is parallel to the tangential flow at the top

of the convection cells. The length of this cell face is typically much smaller than the radial component, suggesting that we observe a diminished asymmetric effect.

However, we actually observe a more prominent lineshift at the limb in both the 3D simulations and the observed spectrum, a pattern also reported by Dravins & Nordlund (1990); the explanation there lays cause on the high horizontal velocities in the upper atmosphere. As for the difference in behaviour between the 3D simulations and the IAG observations, particularly at the limb, it is difficult at this point to determine the degree to which either is more 'accurate' than the other, as there is certainly an array of simplifications and processing techniques for each method, which introduce errors and uncertainty. Nevertheless, the authors of the IAG solar atlas (Reiners et al. 2016) quote accuracy to ±10 m/s, a scale significantly smaller than the magnitude of the effects seen here. If the discrepancy of the bisectors at the limb between the observed and 3D non-LTE synthesised lines is not due to observational issue, then this points to a problem with the modelling at the limb. As the spectrum originating at the solar limb features lines which are, due to geometry, formed higher in the atmosphere, the accuracy of the 3D model at these depths may place a limitation on the agreement between the observational and modelled lines, perhaps due to inaccurate temperatures in the upper atmosphere. Unlike the real Sun, our model atmospheres do not feature the chromosphere, a hotter region which sits above the photosphere. It may be interesting to use a whole atmosphere code (e.g. Gudiksen et al. (2011)) to assess the limb behaviour.

The unusual shape of the limb bisector may be explained by the passage of the 'ray' through multiple regions of up- and down-flow, in a similar mode as the temperature-depth profile of the 3D model discussed earlier. Also in agreement with the Dravins & Nordlund (1990) study of Fe I lines, we see very little influence of non-LTE on the line asymmetry, ie. between panels (b) and (c) there is little difference.

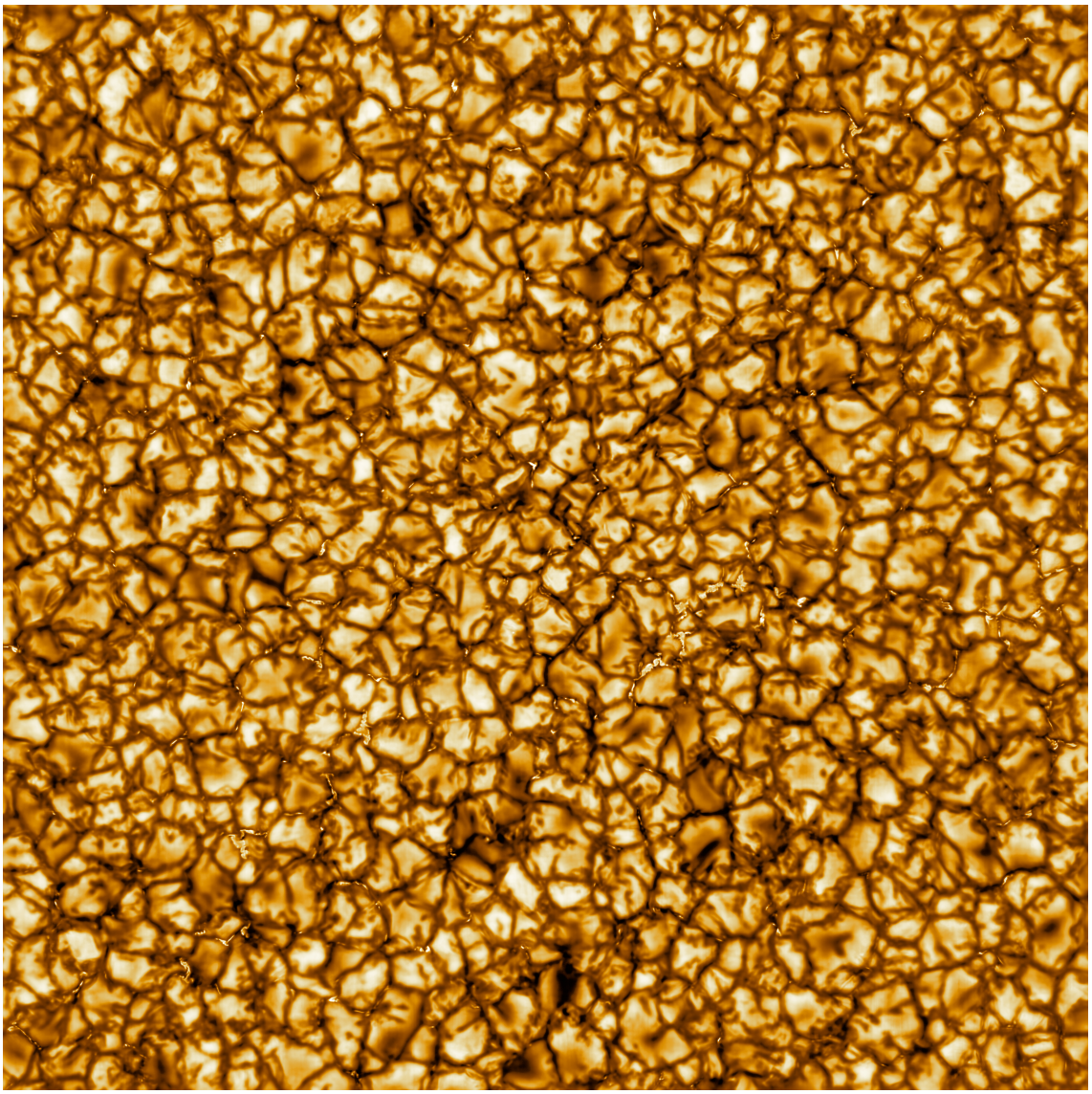

Figure 19: Image of solar granules taken at the wavelength 789nm by the Daniel K. Inouye Solar Telescope. The brighter granules and darker intergranular lanes cover the extent of the Sun's surface; this image covers 35000km x 35000km. Credit: NSO/NSF/AURA.

7.3 Centre to limb abundance variation

Figures 20 and 21 show the relative abundances of solar silicon which have been calculated as described in the Methods section, for the spectral lines at 5645Å, 5701Å and 5772Å. In each case we show the abundance calculated in 1D LTE, and additionally the abundances which correspond to these 1D LTE values with applied 1D non-LTE, 3D LTE and 3D non-LTE abundance differences, using the observed IAG solar spectra. In each figure the abundance is given at each of the six μ angles which were chosen in order to investigate the variance across the solar centre-to-limb.

To analyse the behaviour seen in these figures, it is important to consider that one would expect a 'flat' distribution of relative abundances across the disc, following the prediction from literature (Lodders 2019) that homogenous mixing ensures a constant chemical abundance across the solar surface.

In each of the three diagnostic lines the 1D LTE abundance shows a similar trend - the abundance is calculated to be significantly higher at the limb than at the solar disc centre. For each of the lines, the abundance exhibits a plateau at the angles approaching the disc centre; at the 5645Å line (Fig. 20 top) the abundance at μ angles 0.6, 0.8, 0.9 and 1.0 is close to constant, and the difference in abundance between the limb (μ = 0.2) and this plateau is $\sim$ 0.2 dex. We see a similar trend in the behaviour of the line at 5701 Å (Fig. 20 top), with a smaller centre-limb difference of $\sim$ 0.19 dex.

In the line at 5772Å (Fig. 21) the 1D LTE abundance does not plateau until between μ = 0.8 and the centre, with a difference of $\sim$ 0.23 dex.

Returning again to the line at 5645Å, we see see the effect of the calculated 3D non-LTE abundance differences by looking at the calculated values of abundance which are the sum of these differences and the 1D LTE relative abundance. For this first diagnostic line there is very little variation from centre-to-limb, with just a small increase of $\sim$ 0.01 dex at

the centre. The μ averaged abundance for this line is 7.698 dex.

At 5701Å and 5772Å, we again see an approximately flat distribution across the disc, albeit with a larger increase than the 5645Å case, from limb to centre, of ~ 0.05 dex. The μ averaged abundances for are 7.592 dex and 7.599 dex, respectively.

For all lines, the behaviour of the abundances calculated using the 1D non-LTE differences is more similar to the 1D LTE calculations, but the trend is shallower in each case. For the line at 5645Å, moving from $\mu = 0.2$ to the disc centre, it can be seen that there is a negative trend in calculated relative abundance. From $\mu = 0.6$ to $\mu = 1$ the corrected 1D non-LTE abundances are almost constant, at around 7.65 dex. However, the high abundances in LTE at $\mu = 0.2$ and 0.4 are not corrected to this lower level, as their corresponding abundance differences are not large enough. We see similar trends in the other two lines.

The abundances corresponding to 3D LTE simulations tend to fall between 1D non-LTE and 3D non-LTE values, exhibiting good agreement from centre-to-limb. We can see that in each of the lines, the calculated abundance at the limb is higher in 3D LTE than in 3D non-LTE, and vice versa at the centre. They are 'corrected' less strongly than the 3D non-LTE lines, and in the 5772Å line, exhibit a more 'flat' distribution across the disc than even the 3D non-LTE abundances.

These three figures help us to compare the performance of the three simulation methods in calculating the centre-to-limb silicon abundance in terms of the variation across the disc. It is clear to see in each of the diagnostic lines that the 1D LTE simulations produce abundances which vary significantly across the disc, an obvious issue when faced with our prediction that the abundances be constant over the Sun. The addition of 1D non-LTE abundance differences reduces the variation somewhat, but is still obviously lacking, with a large decreasing trend of abundances when moving from limb to centre. However, the large 3D non-LTE abun-

dance differences serve to convincingly correct the angular bias of the 1D LTE abundances, to produce a largely constant value, particularly in the 5645Å and 5772Å lines.

It is now simpler to understand how the negative to positive transition of abundance differences seen earlier in Fig. 11 are relevant to calculating more accurate final abundances. Indeed, this same transition can be seen when comparing the 1D LTE and 3D non-LTE trends in e.g. Fig 20.

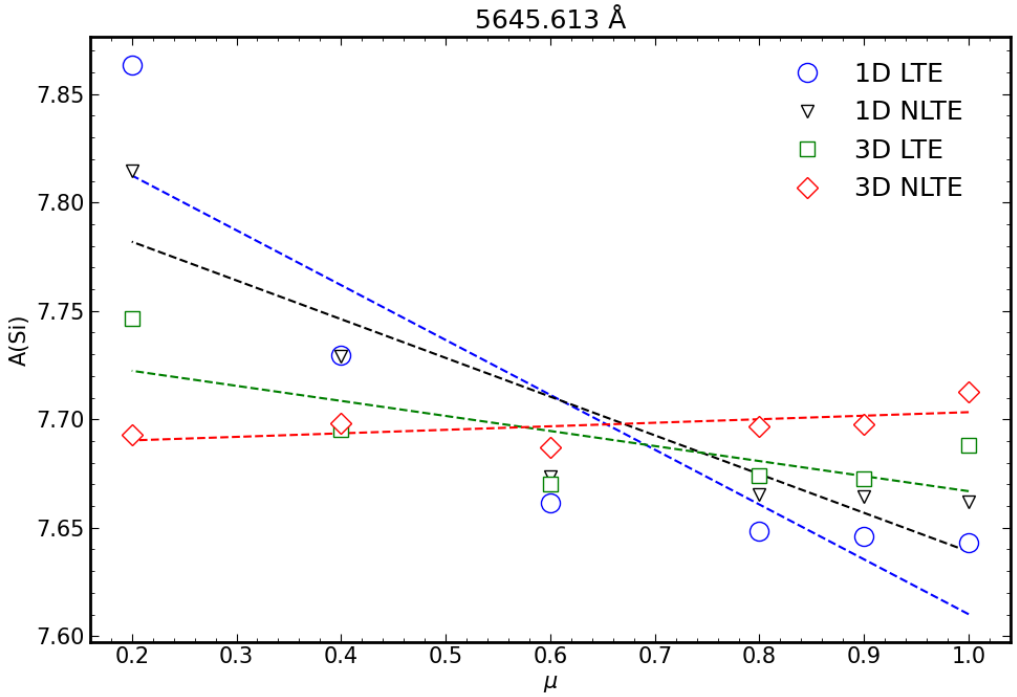

Figure 20: Centre-to-limb variation of Si relative abundance for 1D LTE, 1D non-LTE, 3D LTE and 3D non-LTE corresponds to the line at 5645Å. Also plotted is a least squares linear fit for each set of calculations.

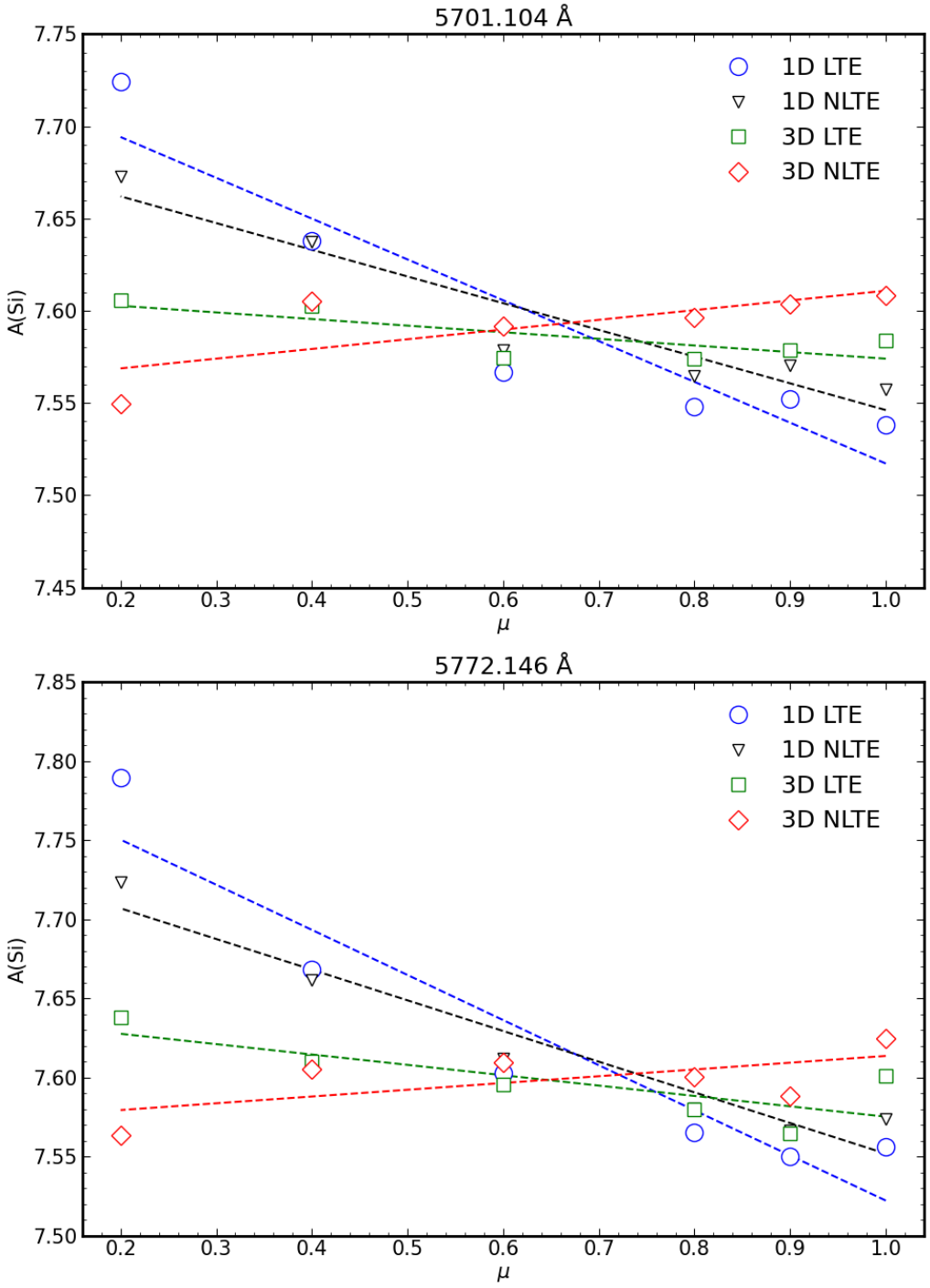

Figure 21: Centre-to-limb variation of Si relative abundance for 1D LTE, 1D non-LTE, 3D LTE and 3D non-LTE, corresponding to the lines at 5701Å (top), 5772Å (bottom). Also plotted is a least squares linear fit for each set of calculations.

7.4 Final abundance estimate

As previously discussed, it is well established that the abundance of a chemical in the solar atmosphere is homogeneous, and we should therefore consolidate the calculations to a single estimate for the whole Sun. To this end, we take a simple mean of the abundances calculated over the 6 μ angles. This gives us a single relative abundance value corresponding to each of our four simulations methods, ie. 1D LTE, 1D non-LTE, 3D LTE and 3D non-LTE for each of the 3 diagnostic line frequencies. A consequence of the μ averaging of abundances is that there is to some degree a dampening of more extreme estimates across the limb, especially in the case of 1D LTE.

Unlike in 1D LTE, 1D non-LTE, and 3D LTE, in 3D non-LTE the calculated abundances are consistent across the solar disc. The μ averaged abundance estimates for the three diagnostic lines are shown in Table 9, alongside the corresponding values from Amarsi & Asplund (2017). The final, line averaged abundance estimate is compared to that of other studies in Table 10. Also shown in Tables 9 and 10 are the abundance values renormalised to the oscillator strengths from Rhodin et al. (2018).

In the analysis of first Scott et al. (2014) and then Amarsi & Asplund (2017), the observed diagnostic lines are given a weight based on their estimated uncertainty, by studying the shape and width of the lines for blends. These weights, shown in Table 9 for the three lines in this study, correlate well with the quality of the line profiles shown in Figs. 23 and 26 (especially with regard to the line at 5645Å, which maintains a noticeable smaller blend even after removal of the larger one). The solar silicon abundance estimate, which is the weighted mean of the abundance calculated at the 6 μ angles and the diagnostic lines at 5645Å, 5772Å and 7034Å is 7.61 dex, with *f-values* of Kurucz (2016) and 7.53 dex with *f-values* from Rhodin et al. (2018). The former figure is ~0.1 dex higher than the standard of the last 20 years (Asplund et al. 2021), but is in good agreement with the recently published study by Magg et al. (2022). The latter abundance value of 7.53 dex is ~0.08 dex lower than the former;

μ	Line λ (Å)		
	5645.613	5701.104	5772.146
1.0	7.643	7.538	7.556
0.9	7.646	7.552	7.550
0.8	7.648	7.548	7.565
0.6	7.661	7.567	7.603
0.4	7.729	7.638	7.668
0.2	7.864	7.724	7.790
Mean	7.699	7.595	7.622

Table 5: Centre-to-limb and mean 1D LTE calculated abundances in dex.

this difference reflects the difference between the $\log gf$ values shown in Table 1.

Overall, the 3D LTE abundance values are very similar to the non-LTE values; the LTE abundance is on average 0.004 dex lower than NLTE across the three lines. The observation that that non-LTE effects are not very significant in Si I lines was also made by Shi et al. (2008), Amarsi & Asplund (2017) and Magg et al. (2022).

μ	Line λ (Å)		
	5645.613	5701.104	5772.146
1.0	7.662	7.557	7.574
0.9	7.664	7.570	7.567
0.8	7.665	7.565	7.580
0.6	7.674	7.579	7.612
0.4	7.729	7.637	7.662
0.2	7.814	7.673	7.724
Mean	7.702	7.597	7.620

Table 6: Centre-to-limb and mean 1D non-LTE calculated relative Si abundances in dex.

μ	Line λ (Å)		
	5645.613	5701.104	5772.146
1.0	7.688	7.584	7.601
0.9	7.673	7.579	7.564
0.8	7.674	7.574	7.580
0.6	7.670	7.575	7.596
0.4	7.695	7.603	7.610
0.2	7.746	7.606	7.638
Mean	7.691	7.587	7.598

Table 7: Centre-to-limb and mean 3D LTE calculated relative Si abundances in dex.

μ	Line λ (Å)		
	5645.613	5701.104	5772.146
1.0	7.713	7.608	7.624
0.9	7.698	7.603	7.588
0.8	7.697	7.596	7.601
0.6	7.687	7.592	7.610
0.4	7.698	7.605	7.605
0.2	7.693	7.550	7.564
Mean	7.698	7.592	7.599

Table 8: Centre-to-limb and mean 3D non-LTE calculated relative Si abundances in dex.

	A(Si)			
λ (Å)	[1]	[2]	Amarsi & Asplund (2017)	Weight
5645.613	7.698	7.625	7.499	1
5701.104	7.592	7.523	7.482	3
5772.146	7.599	7.492	7.553	2

Table 9: Comparison of μ averaged solar silicon abundance estimates in dex for diagnostic lines compared with those of Amarsi & Asplund (2017). [1] - abundances calculated with oscillator strengths from Kurucz (2016), [2] - abundances calculated with oscillator strengths from Rhodin et al. (2018). The suggested weight is based on the quality the line due to blends, as assessed by Scott et al. (2014).

Study	A(Si)
This study	7.61[1], 7.53[2]
Magg et al. (2022)	7.59 ± 0.07
Mashonkina (2020)	7.60
Amarsi & Asplund (2017)	7.51 ± 0.03
Shi et al. (2008)	7.52 ± 0.06
Grevesse & Sauval (1998)	7.55 ± 0.05

Table 10: Line averaged A(Si) estimates in dex from this and previous studies. [1] - abundances calculated with oscillator strengths from Kurucz (2016), [2] - abundances calculated with oscillator strengths from Rhodin et al. (2018).

7.4.1 Plotting lines with the final abundance estimate

With the abundance estimate of A(Si) = 7.61 dex, we compare the line profiles and EWs of a 1D LTE and a 3D non-LTE simulation, illustrated in Figs. 22 and 23. The agreement between the observed and 3D non-LTE lines are very good, despite the small discrepancy at the limb discussed in the section on bisectors, where the observed line is more blueshifted than the simulation.

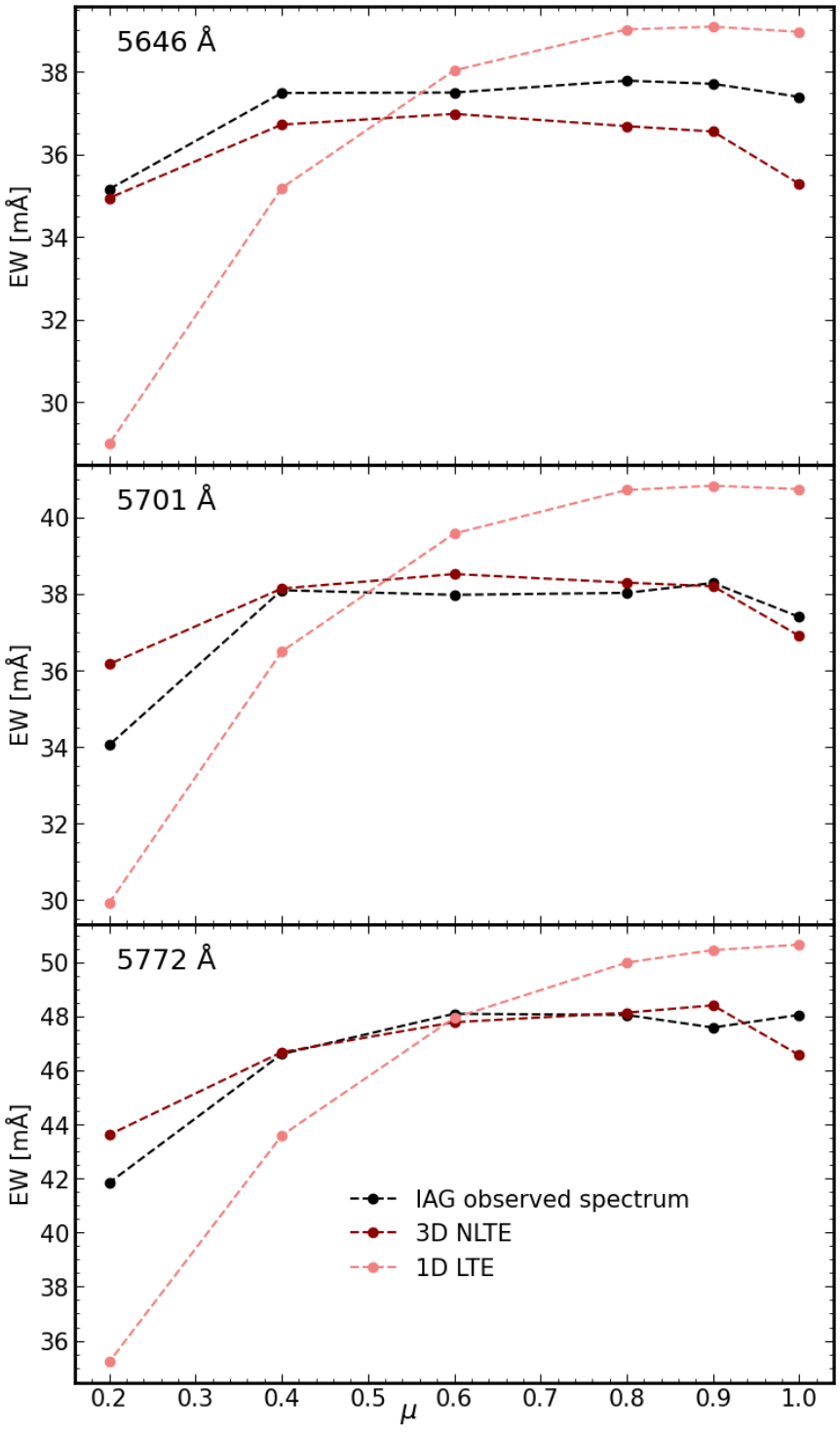

Figure 22: Centre-to-limb variation of line EWs for the observed, 1D LTE and 3D non-LTE spectra, simulated with the estimated solar abundance A(Si) = 7.61 dex.

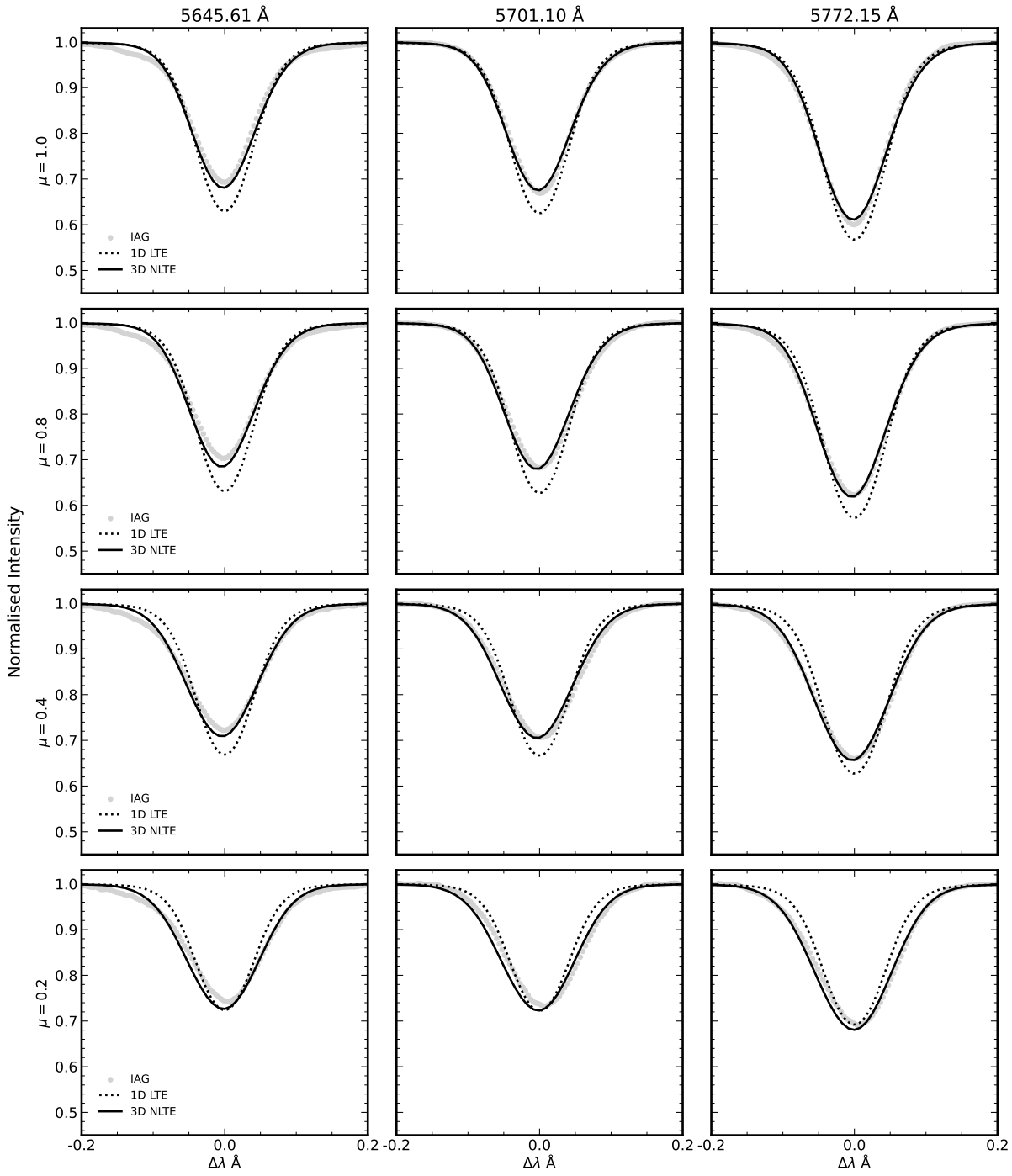

Figure 23: Normalised intensity plots of Si I diagnostic spectral lines: processed IAG solar spectrum, 1D LTE MARCS simulation, 3D non-LTE STAGGER simulation, with A(Si) = 7.61 dex.

8 Discussion

In this discussion section, a number of recent studies which have attempted to estimate the solar silicon abundance are described and compared with this work, both in the results and the details of the investigations. The discussion highlights and elucidates the reasons for the range of solar silicon values which have been calculated in the past few decades.

The first investigation of solar silicon abundance with full 3D non-LTE calculations was Amarsi & Asplund (2017), who found a final abundance estimation of 7.51 ± 0.03 dex., which is the same figure found earlier by Scott et al. (2014), who estimate abundances in 3D LTE. These two studies share the same experimental data; the equivalent widths for the lines used were averages of those measured using the disc centre intensities of the solar atlases Jungfraujoch (Delbouille & Roland 1995) and Kitt Peak (Neckel et al. 1984). Regarding the model atomic data, Amarsi & Asplund (2017) employ a technique in which statistical equilibrium is calculated with reduced model atom of 56 Si I atomic levels and 634 bound-bound transitions. This was achieved by collapsing the fine structure levels of their 'comprehensive' model atom into single levels. They then redistribute the populations on to a more complete model atom with resolved fine structure, and calculate the emergent spectra with this model. In tests on a ⟨3D⟩ model, they report errors in the vertical intensity of less than 0.001 dex when using the reduced model. The comprehensive model atom was made with transitional probabilities from Garz (1973), subsequently renormalised, and with rate coefficients from Belyaev et al. (2014). In their more recent paper (Asplund et al. 2021) the authors consider using the modern gf-values computed by Rhodin et al. (2018), and report that using these values and their original method there would be an upward revision of Si abundance to 7.53 ± 0.03 dex. They do not however choose to keep the Rhodin et al. (2018) *f-values*, as they claim that these imply an ionisation imbalance between Si I and Si II. The authors of this paper use a similar version of the MULTI3D code as used in this work, but without the alterations detailed in Bergemann et al. (2019). Amarsi & Asplund (2017) perform their calculations on six solar snapshots, each

a Cartesian mesh of $240 \times 240 \times 230$, then reduced to $120 \times 120 \times 101$ for non-LTE calculations for computational reasons. They compute radiative transfer and line formation in full 3D.

The most recent investigation into the solar silicon abundance is that by Magg et al. (2022), who report A(Si) = 7.59 ± 0.07. The data and techniques used in this study are similar to that used in this work, but with some notable differences. MARCS is used for 1D simulation, and `STAGGER` for 3D, but in their study ⟨3D⟩ is used in place of full 3D modelling, due to considerations of comparison with future wide-range spectroscopic surveys. Magg et al. (2022) use observations from a 2016 Institute of Astrophysics Göttingen (IAG) solar atlas (Reiners et al. 2016), and for the same reason of compatibility, do not employ spatially resolved intensities on the solar disc, as in this work or by Bergemann et al. (2021). Radiative transfer and statistical equilibrium were calculated with MULTI2.3 which uses accelerated lambda iteration and a long characteristics solver, and spectra synthesised with Turbospectrum. For abundance analysis, they do not compute equivalent widths, but instead fit a grid of model spectra with χ^2 minimisation, as in Bergemann et al. (2021). The model Si atom used by Magg et al. (2022) was similar to that used in this study. However, the *f-values* used in the calculation of statistical equilibrium were different than those used in the line synthesis. Magg et al. (2022) use values from Kurucz (2016) for the former, and values from Rhodin et al. (2018) for the latter.

The other recent non-LTE study of stellar silicon abundances, including the Sun's, is Mashonkina (2020). They use a 1D MARCS atmosphere and the Kitt Peak observational data. Their Si I atomic data consists of 95 levels from NIST (Kramida et al. 2019) and 23 from Kurucz (2016), with *f-values* also from Kurucz (2016). This group do not report a 'final' solar silicon abundance, and do not share the same diagnostic lines as us. However, Magg et al. (2022) calculate A(Si) = 7.60 for Mashonkina (2020), using their common lines.

Our radiative transfer and statistical equilibrium calculations are computed in full 3D model atmospheres with MULTI3D, a short characteristics solver, like Amarsi & Asplund (2017), but unlike Magg et al. (2022). We use only a single solar snapshot instead of an average across multiple as by Amarsi & Asplund (2017). In their Figure 13, Bergemann et al. (2019) show that there is very little difference between spectral lines produced in five different `STAGGER` snapshots, allowing us to be fairly confident that the influence of our choice of a single snapshot is negligible. Our snapshot covers 8x8 Mm, and has a resolution of $240 \times 240 \times 230$, which was reduced in the horizontal axes to $30 \times 30 \times 230$. This is the same configuration as used by Bergemann et al. (2021) in their study of oxygen lines, and who report that the down-scaling to this resolution introduces only 2% difference in line profiles while significantly reducing computational times. In tests made by Amarsi & Asplund (2017), it was found that very minor differences on the vertical intensities were introduced due to down-scaling, and this was still negligible at inclined viewing angles (at most 0.003 dex with a $120^2 \rightarrow 60^2$ resolution change).

We consider now the differences between the observational data used by the studies compared here. In this study a new IAG solar atlas was used, recorded as described in Schäfer et al. (2020). This atlas comes from the same group as the data used by Magg et al. (2022), but with improvements to the experimental setup that fix tracking issues in the former configuration which reportedly introduced errors on the order of 10ms^{-1}. Both this updated atlas and the original (Reiners et al. 2016) are improvements over the Jungfraujoch and Kitt Peak data; IAG report accuracy to 10ms^{-1}, while the Kitt Peak atlases have deviations up to 100ms^{-1}. There were a number of Si I lines which were not used in this study either because of blended features, or because of telluric contamination in the atlas. In comparison to Amarsi & Asplund (2017) and Magg et al. (2022), who use 9 and 8 diagnostic lines respectively, the 3 diagnostic lines used here is perhaps a small sample size with which to take sample. However, as many of these other Si I lines are contaminated by blending, it is difficult to say whether including these lines necessarily improves the accuracy of the results.

Recent efforts to update model atoms for the comprehensive work by Magg et al. (2022), mean that the model atom used in this study is more detailed than that of Mashonkina (2020) and the reduced model used by Amarsi & Asplund (2017). However, a significant factor separating the final abundance estimates of the different studies is the choice of transition frequencies (or oscillator strengths, or *f-values*). With the Kurucz (2016) *f-values*, we estimate a final abundance value (A(Si) = 7.60) which is in close agreement with Mashonkina (2020) (A(Si) = 7.60) and Magg et al. (2022) (A(Si) = 7.59); these studies share the same source of f-values (notwithstanding the *f-values* used for the spectrum synthesis by Magg et al. (2022), from Rhodin et al. (2018)), which for the lines in this study is originally Garz (1973). If the abundances calculated in this study are corrected to use the *f-values* of Rhodin et al. (2018), we find (with the weighting explained above) a final value of A(Si) = 7.53 dex. This figure is now in agreement with the value reported by Asplund et al. (2021), with their corrections to the same *f-values* (A(Si) = 7.53). As discussed earlier, Asplund et al. (2021) do not trust these new *f-values*, and, the results of Rhodin et al. (2018) are not yet published. Therefore, we proceed in the discussion with the results that use Kurucz (2016), which, despite originating from older calculations, are values still used in modern studies. Hopefully publication of the work of Rhodin et al. (2018) and subsequent agreement on its reliability can bring about a convergence of the estimations of the solar abundance of silicon and other chemicals (Palme et al. 2014).

The primary difference between this and previous studies of solar Si abundance is that equivalent widths and abundance values are calculated in full 3D non-LTE across the solar disc, at viewing angles in the range $0.2 \leq \mu \leq 1$, independently. As shown in the results, there is some disagreement with the abundances calculated across the disc, particularly at the limb. In 1D LTE there is a significant overestimation of abundance at the limb, showing that the 1D models are insufficient for spectroscopy at wide viewing angles. As we take a simple average across the μ an-

gles, and then average the values for the three diagnostic lines, we are more reliant on both accurate performance of the statistical equilibrium code and the observational methods, to interpret μ specific intensities accurately, particularly at the limb. From the comparison with EWs and the line profile bisectors, it seems possible that even with the 3D models the methods used here cannot completely accurately synthesise spectra at the solar limb. This may be due to underestimation of the temperature in the upper layers of the atmosphere, where these $\mu = 0.2$ lines form, prompting an overestimation of their strength. However, the discrepancies may be due to the data reduction methods for the observed spectra. There are many unclear sources of error which may enter the calculations, from the effect of data reduction in the observed spectrum to the uncertainty at the limb due to the grid down-sizing. These errors can even differ from the centre-to-limb, making it complicated to unpick the causes of some of the patterns we see in the results. Further, as this is the only study to investigate these lines with the most up to date model atom and observational data across the solar disc with simulations in in full 3D, we cannot make direct line-by-line comparisons. Despite this, it seems that the our final abundance calculations are consistent with studies that use the same source of oscillator strengths.

As silicon is commonly used either as the anchor element, or one of the anchor elements between the meteoric and photospheric abundance scales, changes to the silicon abundance become important when considering the Sun as a whole. Magg et al. (2022) present a new meteoric abundance scale using their value for solar Si abundance (in agreement with A(Si) = 7.61 of this study) as one of the anchor elements, and calculate an updated Z/X ratio which is significantly larger (by 26%) than that of Asplund et al. (2021). This new meteoric abundance was $A(\mathrm{Si})_{\mathrm{met}} = 7.57$. With the metallicity adjustment and new chemical mixture, Magg et al. (2022) calculate standard solar models, and the discrepancy which existed between the canonical photospheric abundances and those inferred by the interior structure of the Sun, evidenced by helioseismic sound speeds, appears to be close to resolved. The revised abundance of oxygen

is the primary driver of this change, but the influence of the refractories is not insignificant.

In the introduction to this work we discussed a number of other astrophysical examples in which the ratio of silicon to some other element is an important factor. In the work of Adibekyan et al. (2012) and Adibekyan et al. (2015), the [Mg/Si] ratio of a star is shown to correlate with its likelihood to host a low mass star. The 1D LTE techniques used in such studies are not suitable for accurate abundance analysis in the Sun, and as the stars in the survey of the latter study are chosen to be within 500K of the solar $T_{\rm eff}$, it is probably not suitable in these cases either. It may be that updated atomic models and 3D non-LTE analysis change the abundances of both metals in such a manner which preserves the ratio, but this again cannot be assumed. This is particularly important if non-LTE introduces opposite strengthening effects in different chemicals Bergemann et al. (2019).

These chemical abundance ratios are defined as relative to the solar abundances as such:

$$[\mathrm{Mg/Si}] = \log_{10}(\mathrm{Mg/Si})_{\rm star} - \log_{10}(\mathrm{Mg/Si})_{\odot} \tag{49}$$

Even beyond the limitations due to the analysis methodology, the dependence of such ratios on the solar abundance estimates mean that changes in the latter can prove important to understanding trends in galactic and stellar evolution. In these investigations on planet-host stars where the [Mg/Si] ratios are compared between stars in the sample, an altered solar abundance ratio gives a constant offset to the distribution. With a constant solar abundance value A(Mg) = 7.55 dex from both Asplund et al. (2021) and Magg et al. (2022), and the change in A(Si) from 7.51 dex (of Asplund et al. (2021) to 7.59 dex estimated by Magg et al. (2022), the [Mg/Si] changes by -0.08 dex. This represents a difference of more than 20% in the abundance ratio for each of the stars.

As discussed, silicon is used either as the only, or as one of the reference elements for meteoric abundances. This means that changes to the canonical silicon abundance can have wide-reaching effects on the studies in solar-system and geophysics which use meteoric abundances.

Many such investigations are made at the Center for Star and Planet Research at the University of Copenhagen; in the work by Connelly et al. (2012), the abundance of uranium isotopes in CI chondrites is used to infer dynamics of the solar protoplanetary disk that led to the formation of the solar system; Bizzarro et al. (2003) use hafnium isotopes in chondrites to gain insight on the Earth's early crust-mantle system. Such studies often use a collection of solar abundances such as Asplund et al. (2009) as a reference for their findings, meaning that updates to these canonical values may require some revision in dependent works. According to Palme et al. (2014), the photospheric Hf abundance is higher than, and in disagreement with the meteoric abundance, which is claimed to have been accurately determined. In cases such as this, re-scaled meteoric abundances may bring photospheric and meteoric measurements into closer alignment.

It is clear that changes to solar abundances can have significant impact, not only for our understanding of the structure of the Sun, but in wider study of star and planet formation. Advances in high performance computing mean that simplifications to 1D LTE may soon be unnecessary, even for large surveys of many stars with different atmospheres. Programs such as the Dispatch Framework (Nordlund et al. 2018), will significantly reduce computational cost of radiative transfer calculation, and enable the addition of magnetohydrodynamic effects in the calculation, enhancing the accuracy of the solar model. Computation time may also be improved with advances in the application of neutral networks; it may soon be possible for techniques such as **SunnyNet**, which Chappell & Pereira (2022) use to compute hydrogen spectra in 3D non-LTE, to be extended to accurately predict the spectra of more complex atoms.

9 Conclusions

In this work we present an investigation into the solar photospheric abundance of silicon, calculating abundances for each of 6 viewing angles across the solar disc with full 3D non-LTE simulations. We synthesise theoretical spectra using a modern model atom, with the MULTI3D radiative transfer and statistical equilibrium code in a 3D `STAGGER` model atmosphere and in a 1D MARCS atmosphere. Abundance differences are calculated with the equivalent width method in 1D non-LTE, 3D LTE and 3D non-LTE.

We use new observational data from the Institute for Astrophysics Göttingen (Schäfer et al. 2020), which features very high resolution spectra at R $\approx$ 900,000, spatially resolved across the solar disc. Three diagnostic lines are identified at 5645Å, 5701Å and 5772Å, while others are rejected due to blending and telluric contamination. We compare line profiles of the diagnostic observed lines and synthesised lines to calculate 1D LTE abundances with the curve of growth method, before using the abundance differences to estimate abundances in 1D non-LTE, 3D LTE and 3D non-LTE, and using two different sources of oscillator strength. Also demonstrated were possible limitations in the calculations at the solar limb caused by the 3D models, using line bisectors to compare the behaviour of the synthesised and observed line profiles across the solar disc, illustrating wavelength shifts and line asymmetries.

We conclude with a final A(Si) = 7.61 dex using older oscillator strengths from Kurucz (2016), and A(Si) = 7.53 dex using recent, experimental, but unpublished oscillator strengths from Rhodin et al. (2018). The values are calculated using the mean of the abundances calculated for each μ angle and with a weighted mean over the diagnostic lines, based on their adjudged quality. Finally, we compare these results to those of some similar studies of photospheric abundance, finding agreement with the most recent (Magg et al. 2022), (Mashonkina 2020) studies with the former A(Si) value, and agreement with renormalised Asplund et al. (2021) calculations, with the latter A(Si) value. It is shown how sig-

nificant differences in the oscillator strengths in the literature have major influence over the estimated silicon abundance. These results are placed in the context of the solar abundance problem at large and with agreement with meteoric abundance and solar models.

In general there was an excellent consistency in equivalent widths calculated in 3D non-LTE with observational data, and abundances which are largely consistent across the solar disc. This is not achieved with modelling in 1D LTE, 1D non-LTE, or 3D LTE, highlighting the value of realistic 3D non-LTE modelling in the analysis and interpretation of astronomical spectra.

Acknowlegments

Many thanks to my supervisors, Maria Bergemann, Åke Nordlund, and Troels Haugbølle for their guidance and support; to Richard Hoppe, for plenty of computational expertise; to Poul Damgaard, Martin Pessah, and the students at the NBI for providing an excellent working environment, and for their help. Thanks also to Ansgar Reiners and Monika Ellwarth for their generosity and helpful communication regarding the IAG observational data.

References

Adelberger, E. G., García, A., Robertson, R. H., et al. 2011, Reviews of Modern Physics, 83, 195

Adibekyan, V., Santos, N., Figueira, P., et al. 2015, Astronomy & Astrophysics, 581, L2

Adibekyan, V. Z., Sousa, S., Santos, N., et al. 2012, Astronomy & Astrophysics, 545, A32

Amarsi, A. & Asplund, M. 2017, Monthly Notices of the Royal Astronomical Society, 464, 264

Asplund, M. 2000, arXiv preprint astro-ph/0005322

Asplund, M., Amarsi, A., & Grevesse, N. 2021, arXiv preprint arXiv:2105.01661

Asplund, M., Grevesse, N., Sauval, A. J., & Scott, P. 2009, Annual review of astronomy and astrophysics, 47, 481

Belyaev, A. K., Yakovleva, S. A., & Barklem, P. S. 2014, Astronomy and Astrophysics, 572, A103

Bergemann, M. 2014, in Determination of Atmospheric Parameters of B-, A-, F-and G-Type Stars (Springer), 187–205

Bergemann, M., Collet, R., Amarsi, A. M., et al. 2017, The Astrophysical Journal, 847, 15

Bergemann, M., Gallagher, A. J., Eitner, P., et al. 2019, Astronomy & Astrophysics, 631, A80

Bergemann, M., Hoppe, R., Semenova, E., et al. 2021, Monthly Notices of the Royal Astronomical Society, 508, 2236

Bergemann, M., Kudritzki, R.-P., Würl, M., et al. 2013, The Astrophysical Journal, 764, 115

Bergemann, M. & Nordlander, T. 2014, Determination of Atmospheric Parameters of B-, A-, F-and G-Type Stars, 169

Bizzarro, M., Baker, J. A., Haack, H., Ulfbeck, D., & Rosing, M. 2003, Nature, 421, 931

Brugamyer, E., Dodson-Robinson, S. E., Cochran, W. D., & Sneden, C. 2010, in AAS/Division for Planetary Sciences Meeting Abstracts, Vol. 42, AAS/Division for Planetary Sciences Meeting Abstracts #42, 27.26

Caffau, E., Ludwig, H.-G., Steffen, M., Freytag, B., & Bonifacio, P. 2010, Solar Physics, 268, 255–269

Chappell, B. A. & Pereira, T. M. 2022, Astronomy & Astrophysics, 658, A182

Clayton, D. D. 1983, 7 (University Press)

Collins, G. W. et al. 1989, New York, WH Freeman and Co., 1989, 512

Connelly, J. N., Bizzarro, M., Krot, A. N., et al. 2012, Science, 338, 651

Delbouille, L. & Roland, C. 1995, in Laboratory and Astronomical High Resolution Spectra, Vol. 81, 32

Dravins, D. & Nordlund, Å. 1990, Astronomy and Astrophysics, 228, 184

Eddy, J. A. 1979, A new sun: the solar results from SKYLAB, Vol. 402 (Scientific and Technical Information Office, National Aeronautics and Space . . .)

Emerson, D. 1998, Interpreting astronomical spectra (John Wiley & Sons)

Garz, T. 1973, Astronomy and Astrophysics, 26, 471

Gehren, T., Butler, K., Mashonkina, L., Reetz, J., & Shi, J. 2001, Astronomy & Astrophysics, 366, 981

Goldschmidt, V. M. 1937, Journal of the Chemical Society (Resumed), 655

Gray, D. F. 2005, Publications of the Astronomical Society of the Pacific, 117, 711

Grevesse, N. & Sauval, A. 1998, Space Science Reviews, 85, 161

Gudiksen, B. V., Carlsson, M., Hansteen, V. H., et al. 2011, Astronomy & Astrophysics, 531, A154

Gustafsson, B., Edvardsson, B., Eriksson, K., et al. 2008, Astronomy & Astrophysics, 486, 951

Haywood, M. 2008, Astronomy & Astrophysics, 482, 673

Henyey, L., Vardya, M., & Bodenheimer, P. 1965, The Astrophysical Journal, 142, 841

Hosaka, J., Ishihara, K., Kameda, J., et al. 2006, Physical Review D, 73, 112001

Howes, L. M., Asplund, M., Keller, S. C., et al. 2016, Monthly Notices of the Royal Astronomical Society, 460, 884

Kobayashi, C. 2016, Nature, 540, 205

Kobayashi, C., Karakas, A. I., & Lugaro, M. 2020, The Astrophysical Journal, 900, 179

Kramida, A., Yu. Ralchenko, Reader, J., & and NIST ASD Team. 2019, NIST Atomic Spectra Database (ver. 5.7.1), [Online]. Available: `https://physics.nist.gov/asd` [Sun May 01 2022]. National Institute of Standards and Technology, Gaithersburg, MD.

Kurucz, R. 2016, Kurucz database. http://kurucz.harvard.edu/atoms/1400/. Assessed on or before 20 May 2022

Leenaarts, J. & Carlsson, M. 2009, in The Second Hinode Science Meeting: Beyond Discovery-Toward Understanding, Vol. 415, 87

Lind, K., Amarsi, A., Asplund, M., et al. 2017, Monthly Notices of the Royal Astronomical Society, 468, 4311

Lodders, K. 2019, arXiv preprint arXiv:1912.00844

Lodders, K., Palme, H., & Gail, H.-P. 2009, arXiv preprint arXiv:0901.1149

Magg, E., Bergemann, M., Serenelli, A., et al. 2022, arXiv preprint arXiv:2203.02255

Magic, Z., Collet, R., Asplund, M., et al. 2013, Astronomy & Astrophysics, 557, A26

Mashonkina, L. 2020, Monthly Notices of the Royal Astronomical Society, 493, 6095

Mihalas, D. 1978, San Francisco: WH Freeman

Neckel, H. et al. 1984, Solar Physics, 90, 205

Nordlund, Å., Ramsey, J. P., Popovas, A., & Küffmeier, M. 2018, Monthly Notices of the Royal Astronomical Society, 477, 624

Nordlund, Å., Stein, R. F., & Asplund, M. 2009, Living Reviews in Solar Physics, 6, 1

Palme, H., Lodders, K., & Jones, A. 2014, Planets, Asteriods, Comets and The Solar System, Volume 2 of Treatise on Geochemistry (Second Edition). Edited by Andrew M. Davis. Elsevier, 2014., p. 15-36, 2

Reggiani, H., Schlaufman, K. C., Casey, A. R., & Ji, A. P. 2020, The Astronomical Journal, 160, 173

Reiners, A., Mrotzek, N., Lemke, U., Hinrichs, J., & Reinsch, K. 2016, Astronomy & Astrophysics, 587, A65

Rhodin, A. P., Hartman, H., Nilsson, H., & Jönsson, P. 2018

Robinson, S. E., Laughlin, G., Bodenheimer, P., & Fischer, D. 2006, The Astrophysical Journal, 643, 484

Rutten, R. J. et al. 1995, Radiative transfer in stellar atmospheres (Citeseer)

Sánchez-Bajo, F., Vaquero, J., & Montero, M. R. 2002, European journal of physics, 23, 323

Schäfer, S., Royen, K., Zapke, A. H., Ellwarth, M., & Reiners, A. 2020, in Ground-based and Airborne Instrumentation for Astronomy VIII, Vol. 11447, SPIE, 2187–2208

Scott, P., Grevesse, N., Asplund, M., et al. 2014, Astronomy & Astrophysics, 573, A25

Serenelli, A. 2016, The European Physical Journal A, 52

Shi, J., Gehren, T., Butler, K., Mashonkina, L., & Zhao, G. 2008, Astronomy & Astrophysics, 486, 303

Thiabaud, A., Marboeuf, U., Alibert, Y., et al. 2014, Astronomy & Astrophysics, 562, A27

Woosley, S. E. & Weaver, T. A. 1995, The Astrophysical Journal Supplement, 101, 181

Yong, D., Norris, J. E., Bessell, M. S., et al. 2012, The Astrophysical Journal, 762, 26

A Appendix

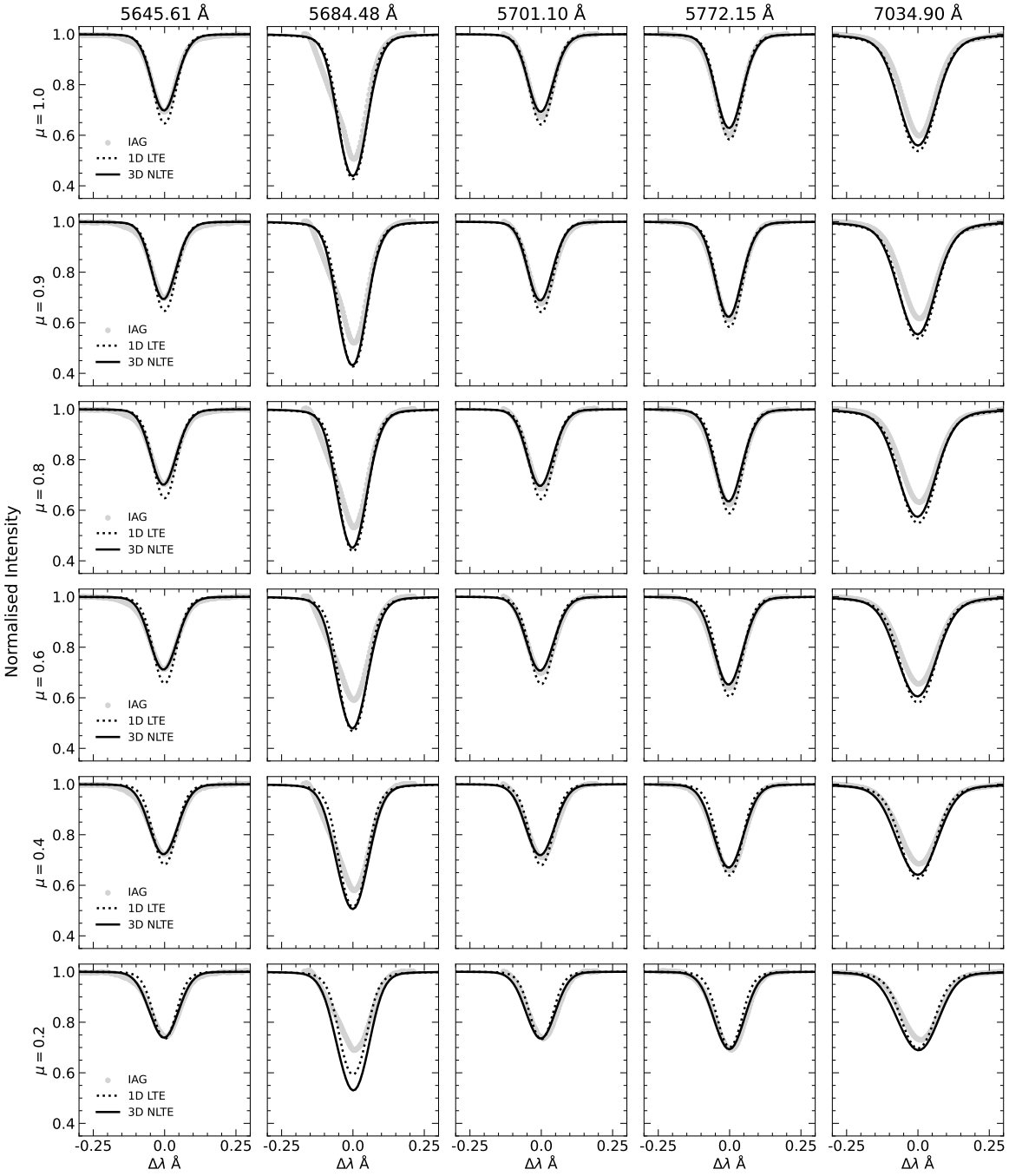

Figure 24: Normalised intensity plots of Si I spectral lines: processed IAG solar spectrum, 1D LTE MARCS simulation, 3D non-LTE STAGGER simulation. Simulations calculated with A(Si)=7.56 and oscillator strengths from Kurucz (2016).

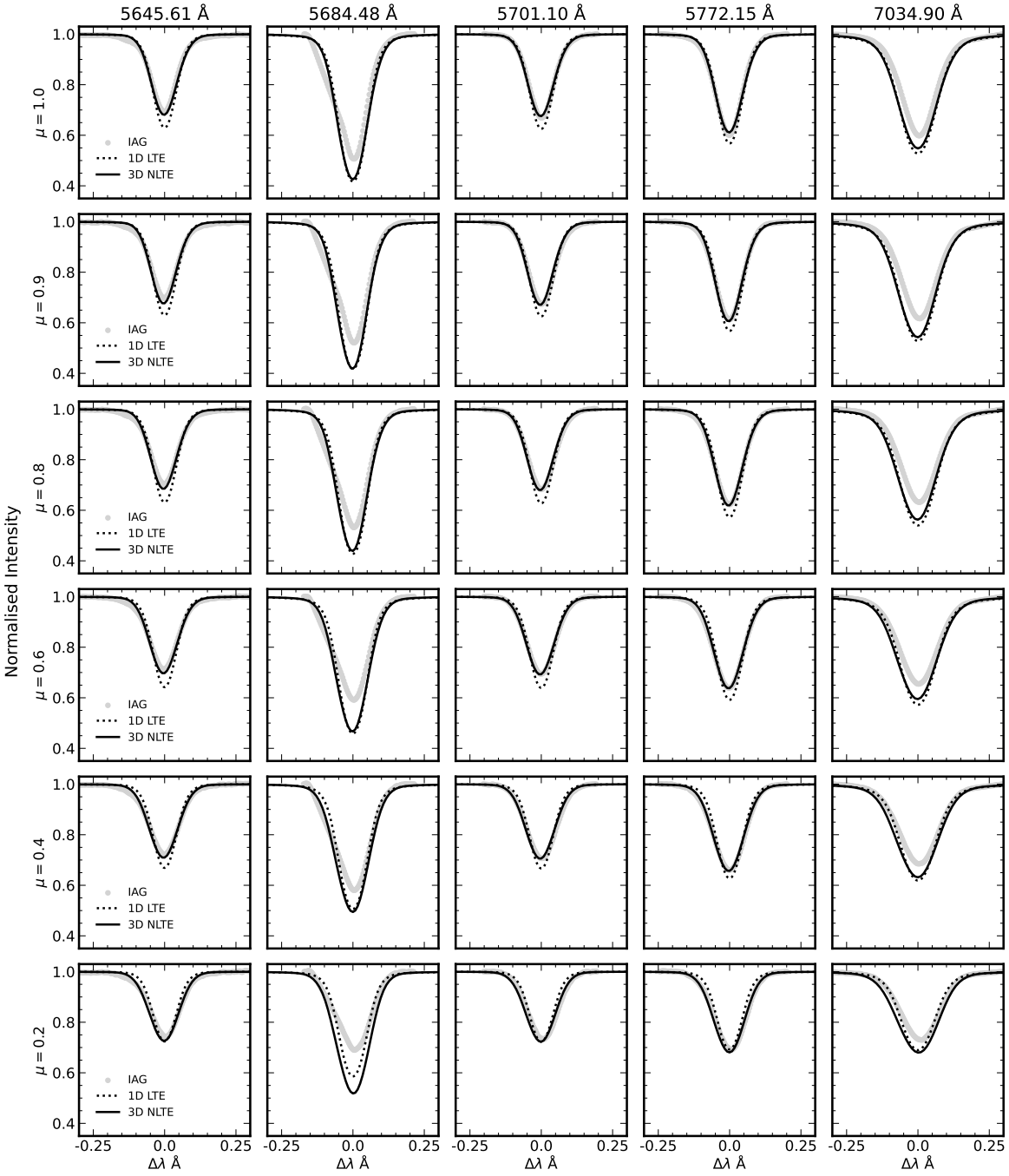

Figure 25: Normalised intensity plots of Si I spectral lines: processed IAG solar spectrum, 1D LTE MARCS simulation, 3D non-LTE STAGGER simulation. Simulations calculated with A(Si)=7.61 and oscillator strengths from Kurucz (2016).

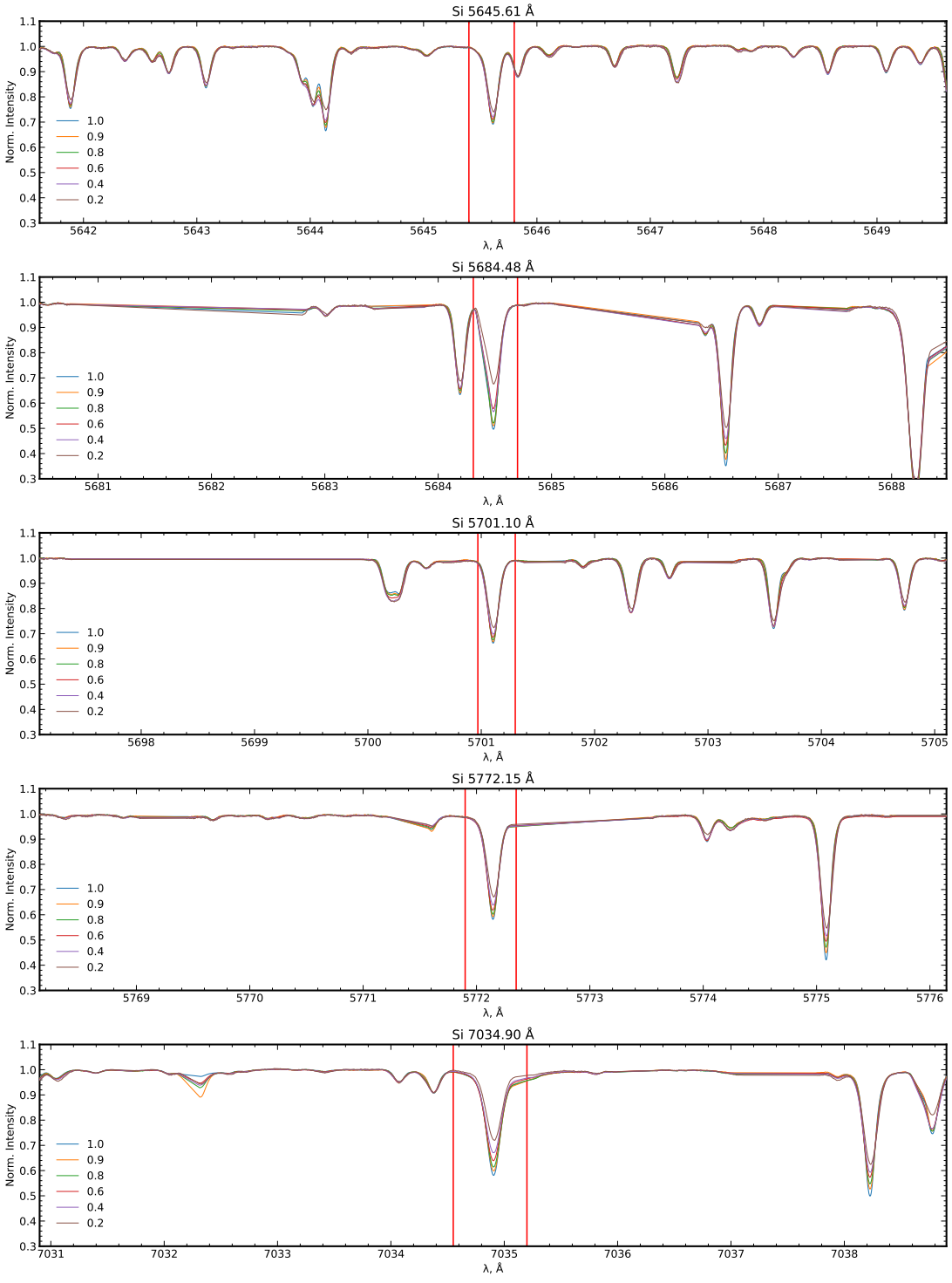

Figure 26: Spatially resolved observed spectra from IAG before deblending and renormalisation.